Cell Biol Toxicol (2025) 41:67
https://doi.org/10.1007/s10565-025-10013-x

RESEARCH

Targeting B4GALT3 in BMSCs-EVs for Therapeutic Control of HCC via NF-κB pathway inhibition

Juncheng Guo · Kaiqiong Wang · Qigang Sun · Jun Liu · Jinfang Zheng

Received: 6 November 2024 / Accepted: 12 March 2025

Abstract Examining the communications in the tumor microenvironment (TME) specific to hepatocellular carcinoma (HCC), this exploration looks into the role played by beta-1,4-Galactosyltransferase III (B4GALT3) in bone marrow mesenchymal stromal cell-derived extracellular vesicles (BMSCs-EVs) regarding the NF-κB pathway and the triggering of cancer-associated fibroblasts (CAF). Through a multidisciplinary approach combining transcriptome sequencing, bioinformatic analysis, and various experimental models, the involvement of B4GALT3 in regulating CAF activity by modulating NF-κB signaling was brought to light in our study. The outcomes suggest that targeting B4GALT3 could impede HCC cell migration and invasion, promote apoptosis, and dampen tumor progression and metastasis, offering novel insights into potential therapeutic strategies for combating HCC.

Keywords Hepatocellular Carcinoma · Bone Marrow Mesenchymal Stromal Cells · Extracellular Vesicles · Tumor Microenvironment · Beta-1

Supplementary Information The online version contains supplementary material available at https://doi.org/10.1007/s10565-025-10013-x.

J. Guo · K. Wang · Q. Sun · J. Liu · J. Zheng (✉)
Department of Hepatobiliary Surgery, Hainan General Hospital, No.19 Xinhua Road, Xiuying District, Haikou 570311, Hainan Province, China
e-mail: zhengjfhnyxy@163.com

Introduction

A commonly observed malignant tumor worldwide, hepatocellular carcinoma (HCC) demonstrates high rates of occurrence and fatality (Zuo et al. 2020; Liu et al. 2022; Zhu et al. 2022). The pathogenesis of HCC is complex and closely related to genetic, environmental factors, and lifestyle (Chidambaranathan-Reghupaty et al. 2021, Llovet et al. 2021, Konyn et al. 2021). HCC is a lethal disease with a high prevalence and poor prognosis. Among liver cancers, HCC is the primary malignant tumor, accounting for 75%−85% of cases. A vast majority of HCC occurrences, exceeding 80%, exhibit profound hepatic fibrosis, incited by the activation, propagation, and aggregation of fibroblasts (Bray et al. 2018).

Typically diagnosed in advanced stages, the treatment options for patients at this point are very limited, resulting in poor prognosis (Vogel et al. 2022, Chidambaranathan-Reghupaty et al. 2021, Llovet et al. 2021). While traditional treatment methods such as surgical resection, radiotherapy, and chemotherapy show significant efficacy in early-stage HCC, their effectiveness is limited in advanced-stage patients (Hanson et al. 2020). Furthermore, owing to the elevated recurrence frequency of HCC and the resistance to chemotherapy, treatment results are frequently less than satisfactory (Hack et al. 2020; Nevola et al. 2023; Zhang et al. 2021a, b). Therefore, venturing into new treatment methodologies is crucial for enhancing survival rates and improving the quality

Published online: 05 April 2025

of life for those afflicted with HCC. Notably, cutting-edge approaches focusing on the tumor microenvironment (TME) have garnered attention within the HCC research community.

The recent years have witnessed a surge in interest towards the TME's role in tumor growth and therapeutic interventions (Yang et al. 2021, Khan et al. 2023, Huang et al. 2022a, b, c). Comprising tumor cells, adjacent non-tumor cells (including fibroblasts, immune cells, and vascular cells), and an extracellular matrix, the TME is a complex ecosystem (Chen et al. 2020). A significant feature of the TME is the extensive activation of cancer-associated fibroblasts (CAFs), which produce a range of cytokines, chemokines, and growth factors that directly or indirectly support cancer cells (Affo et al. 2017; Yin et al. 2019). Within this microenvironment, CAFs play a crucial role (Mao et al. 2021a, b; Luo et al. 2022; Biffi and Tuveson 2021). CAFs interact with tumor cells by secreting growth factors, cytokines, and matrix metalloproteinases, thereby promoting tumor growth, invasion, and metastasis (Mao et al. 2021a, b; Huang et al. 2022a, b, c; Li et al. 2022a, b). CAFs also modulate the immune microenvironment of the TME, influencing the immune evasion and drug resistance of tumors (Mao et al. 2021a, b; de Visser and Joyce 2023; Biffi and Tuveson 2021). Therefore, delving into the biological behaviors exhibited by CAFs amidst the TME is essential for gaining insights into the pathways of tumor evolution and devising novel therapeutic schemes.

Recent studies have demonstrated a close interaction between mesenchymal stem cells (MSCs) and CAFs, with extracellular vesicles (EVs) derived from MSCs exhibiting similar functions to their parental MSCs. These EVs can transfer various bioactive molecules to CAFs (Zhang 2023, Eiro et al. 2021, Zheng et al. 2019). Moreover, bone marrow mesenchymal stem cell-derived EVs (BMSCs-EVs) have been reported to inhibit HCC progression (Deng et al. 2021; Zhang et al. 2022). Notably, inhibition of beta-1,4-Galactosyltransferase III (B4GALT3) has been shown to activate CAFs, promoting HCC progression and metastasis (Fang et al. 2018).

Bone mesenchymal stromal cells (BMSCs), a type of multipotent cell, have shown potential in treating HCC, drawing widespread attention in the academic community (Abd-Allah et al. 2014). However, it is widely believed that the functionality of BMSCs primarily relies on the cell factors, growth factors, and EVs released through paracrine signaling (Zheng et al. 2019; Gu et al. 2021). BMSCs-EVs, as a crucial intercellular communication tool, have garnered significant interest in oncology research in recent years (Guo et al. 2020; Zhou et al. 2023; Kletukhina et al. 2022). These BMSCs-EVs can transport various biomolecules, including proteins, lipids, mRNA, and miRNA, influencing tumor development through interactions with target cells (Xiong et al. 2021; Wang et al. 2023; Huang et al. 2022a, b, c). In the field of HCC therapy, BMSCs-EVs demonstrate promising prospects as drug-delivery vehicles that can directly target and inhibit HCC (Yang et al. 2022). Furthermore, BMSCs-EVs possess the ability to promote apoptosis in HCC cells and inhibit tumor growth (Deng et al. 2021). Studies indicate that BMSCs-EVs suppress HCC cell proliferation by downregulating c-FLIP expression, increasing TRAIL levels, and promoting apoptosis (Deng et al. 2021). Therefore, comprehensive research into the functions and mechanisms of BMSCs-EVs is crucial for developing novel strategies for HCC treatment.

The NF-κB signaling pathway is a pivotal cellular signaling cascade that is crucial in regulating inflammation, immune response, and cell survival (Yu et al. 2020; Hwang et al. 2020). Irregular triggering of the NF-κB signaling pathway is closely correlated with the tumor proliferation, invasion, metastasis, and chemoresistance during tumorigenesis and progression (Zhao et al. 2021; Hayes et al. 2020; Peng et al. 2020). This pathway can promote the survival and dissemination of malignant cells in the TME through various mechanisms (Lazarian et al. 2020). In HCC, the stimulation of NF-κB is significantly correlated with tumor deterioration and unfavorable prognosis (Zhang et al. 2021a, b; Vucur et al. 2023; Lin et al. 2021). Therefore, the potential therapeutic efficacy of targeting the NF-κB signaling pathway in cancer treatment is increasingly recognized, with the suppression of its activity being vital in slowing down the progression of HCC.

B4GALT3 is an enzyme responsible for synthesizing poly-N-acetyllactosamine, and its downregulation is closely linked to tumor progression (Chen et al. 2014; Liu et al. 2018). Investigations have revealed that exosomal miR-1247-3p derived from tumors directly aims at B4GALT3, triggering the β1-integrin/NF-κB cascade, subsequently activating

CAFs, thus fostering the progression and metastasis of HCC (Fang et al. 2018). However, no study has yet indicated whether there is a correlation between the restraining influence of BMSCs-EVs on HCC and the control of the B4GALT3/NF-κB signaling pathway in activating CAFs.

The main focus of this research is to investigate extensively the involvement and process of BMSCs-EVs in the advancement of HCC. Particularly, we focus on the impact of B4GALT3 in BMSCs-EVs on the NF-κB signaling pathway and how this influence modulates the growth and metastasis of HCC through regulating CAFs in the TME. The outcomes of this exploration are projected to present a innovative theoretical underpinning and molecular markers for the detection and care of HCC. Seeking a profound understanding of how BMSCs-EVs function within the TME, our aspiration is to fashion more potent treatment techniques for enhancing the prognosis and quality of life for individuals suffering from HCC.

Materials and methods

Isolation of BMSCs

Human BMSCs (HUXMA-01001, Cyagen, USA) were maintained in DMEM medium (12,430,047, Gibco, USA) supplemented with 10% fetal bovine serum (FBS) (12,483,020, Gibco, USA) and 1% penicillin/streptomycin (15,070,063, Gibco, USA) within a 37 °C incubator with 5% carbon dioxide. Cultivation of BMSCs in the third segment was carried out in DMEM encompassing 10% FBS until they achieved 80% confluence. To induce adipocytes, BMSCs underwent exposure to 1 μL/L dexamethasone (ST1254-50 mg, Beyotime, China), 0.5 μL/L isobutylmethylxanthine (410,957, Merck, USA), 60 μL/L indomethacin (SF6804-25 mg, Beyotime, China), and 10 μL/L insulin (P3376-100 IU, Beyotime, China). To promote osteogenesis, BMSCs were co-treated with 0.1 μL/L dexamethasone, 10 mmol/L glycerol 3-phosphate (G5251, Merck, USA), and 50 μL/L ascorbic acid (1,043,003, Merck, USA). After 3 weeks of induction, differentiation into adipocytes and osteoblasts was assessed using an Oil Red O staining kit (C0157S, Beyotime, China) and Alizarin Red staining (C0148S, Beyotime, China), respectively.

In the third passage, BMSCs were dissociated using 0.25% trypsin–EDTA (25,200,072, Gibco, USA) and enumerated. Nearly 1×10^6 cells were reconstituted in 200 μL of Fluorescence-activated cell sorting (FACS) buffer (660,585, BD Biosciences, USA). Afterward, the cells were chilled on ice and administered with 2 μL of fluorescent antibodies in conjunction with isotype controls, all throughout a period lasting 30 min. Following this, bone marrow stem cells (BMSCs) underwent rinsing with FACS solution, were then treated with 10% formalin (R04587, Merck, United States), and the proportion of positive antigens was assessed utilizing the BD FACSCalibur flow cytometer (BD Biosciences, USA). Antibodies used included CD90 (ab307736, 1:500), CD70 (ab77868, 1:500), and CD45 (ab10558, 1:1000) from Abcam, USA (Deng et al. 2021).

Isolation and recognition of BMSCs-EVs

BMSCs were seeded in a 6-well plate and allowed to adhere for 24 h. The cells were rinsed with serum-free α-MEM (A1049001, Gibco, USA) and cultured in fresh serum-free α-MEM for another 24 h. Centrifugation at 2000 g led to the retrieval of the conditioned medium (CM). Ultracentrifugation was employed to isolate BMSCs-EVs in the CM. In brief, removal of cellular debris was achieved through centrifugation at 7000×g for 20 min. Subsequently, microvesicles were pelleted at 16,500×g over a period of 2 h at 4 °C. Following a 100,000×g separation for 2 h at 4 °C, EVs underwent a rinse using PBS and underwent a subsequent centrifugation at 100,000×g for an additional 2 h. GW4869 (HY-19363, MedChemexpress, USA), a commonly used neutral sphingomyelinase inhibitor at a concentration of 10 μM, was utilized to inhibit EVs generation and affect the composition and biological activities of EVs membranes (Andreeff et al. 1987; Dorronsoro et al. 2021).

Transmission electron microscopy (TEM) was employed to identify EVs: A copper grid was utilized to receive 20 μL of EVs, which were allowed to settle for 3 min, after which excess liquid was removed using filter paper. Subsequently, 30 μL of phosphotungstic acid solution (pH 6.8) (79,690, Merck, USA) was added. Subsequently, the grid underwent air-drying subsequent to a 5-min exposure at ambient temperature, leading to examination using a transmission electron microscope (JEOL's JEM-1011 model based

in Tokyo, Japan) with an accelerating voltage set at 80 kV, and visuals were obtained via a side-mounted Camera-Megaview III (Soft Imaging System, Muenster, Germany).

The size and quantity of EVs were measured through the use of nanoparticle tracking analysis (NTA): Suspended in PBS, the EVs samples were diluted by a factor of 500 using Milli-Q water and were carefully introduced into the sample space of a NanoSight LM10 tool from the UK's Malvern facility with the aid of a sterile syringe, ensuring the absence of bubbles until the space was fully occupied. Utilization of NanoSight software 2.3 from Malvern, UK, was crucial during the video analysis procedure. Specifically, a gain setting of 6.0 and a threshold value of 11 facilitated the monitoring of particle movement, leading to the generation of profiles depicting concentration and size distribution for the diluted samples. Consequently, the calculation of the EVs' initial concentration was made based on the dilution factor.

The surface markers of EVs were identified using Western blot (WB): Two sample groups were established: the GW4869 group (where EV activity was inhibited using GW4869 as a control group) and the BMSCs-EVs group (used to verify EV extraction purity). EVs suspended in RIPA lysis buffer (89,901, Thermo, USA) were probed for specific markers such as CD9, CD63, TSG101, and HSP70, with Calnexin serving as a negative control, utilizing rabbit anti-CD9 (ab307085, 1:1000), anti-CD63 (ab134045, 1:1000), anti-TSG101 (ab125011, 1:1000), anti-HSP70 (ab2787, 1:1000), and anti-Calnexin (ab22595, 1:1000) antibodies from abcam (UK) (Li et al. 2021; He et al. 2020; Gangadaran et al. 2017; Zhou et al. 2019). Every trial was conducted thrice.

Silence and Overexpression of B4GALT3 through Lentivirus Construction and Transfection.

Initially, formulated were three different sets of sequences to target B4GALT3, where a sequence without any interfering elements was utilized as a control (sh-NC). Table S1 contains the primer sequences, and GenePharma® from Shanghai, China, synthesized the oligonucleotides. Utilization of the lentivirus packaging system pLKO.1 involved the co-transfection of the packaged virus and target vector into 293 T cells (H4-1601, Cyagen, USA) using Lipofectamine 2000 (Invitrogen, USA) once the cellular confluence reached 80–90%. Upon completing a 2-day cell incubation, the fluid medium was procured, subjected to centrifugal force, and detected to harbor viral elements. The viruses proliferating exponentially were collected, and the viral potency was ascertained. Manufactured and packaged by Genechem located in Shanghai, China, the lentiviral vector designated LV-B4GALT3 was tailored for the amplification of B4GALT3 expression. After entering the logarithmic stage, the cells underwent digestion and transfer using trypsin, leading to a concentration of 5×10^4 cells/mL of BMSCs, which were subsequently placed in a 6-well tray, containing 2 mL per well. Each lentivirus (MOI = 10, viral titer of 1×10^8 TU/mL) was introduced into the cellular medium and cultured for a period of 48 h. The process of selecting stable cell lines involved the use of 2 μg/mL puromycin (UC0E03, Sigma-Aldrich, Germany) for a period of 14 days (Zhang et al. 2019; Wang et al. 2020; Ni et al. 2021; Shi et al. 2020).

Grouping of BMSCs-EVs Co-culture with CAFs cells

Human CAFs cells (SNP-H067, SUNNCELL) were co-cultured with BMSCs-EVs for 24 and 48 h in DMEM medium containing 10% FBS and 1% penicillin/streptomycin. The co-cultures were incubated at 37 °C with 5% CO_2. The co-culture experiments of EVs with CAFs cells were divided into 6 groups, with detailed procedures outlined in Table S2. CAFs cells were treated with 0.5 μM of the NF-κB activator Diprovocim (TNFα; HY-123942, MedChemexpress, USA) for 24 h (Chen et al. 2017; Peng et al. 2023).

Observation of the uptake of EVs by CAFs using fluorescence microscopy

CAFs were pre-seeded onto glass coverslips in a 24-well plate. Each well was filled with a cell suspension composed of 5×10^4 cells per well. Upon the adherence of CAFs, pre-stained EVs supernatant was added, and co-cultured for 24 h. Dil dye (C1036, Beyotime, China) was mixed with 40 μg of EVs to reach a last level of 25 μM. Subsequent to a 30-min room temperature incubation, the undyed molecules were separated by swift centrifugation. Subsequently, the cells received three PBS washes and were subsequently immobilized with 4% paraformaldehyde (PFA, AR1068, Boster, China) for 30 min. Ultimately, the staining of cell nuclei with DAPI (C1005,

Beyotime, China) lasted 30 min, and CAFs were visualized at × 400 magnification applying a fluorescence microscope equipped with a camera (BX53, Olympus, Japan). Blue fluorescence indicated the CAFs nuclei, while red fluorescence indicated Dil. Results were presented as the ratio of Dil fluorescence area to DAPI fluorescence area, computed utilizing ImageJ software developed by the National Institutes of Health in the United States. Examination of each cell involved 5 image sections and the observation of 6–10 fields chosen at random (Cui et al. 2021; Xiong et al. 2022). The experiment was replicated on three occasions.

Grouping of CAFs and HCC Cell Co-culture experiments

Co-culture of CAFs with HCC Cells: Normal liver cell line THLE-2 (MZ-8312) and liver cancer cell lines Huh-7 (MZ-0095), SNU-182 (MZ-2656), and JHH7 (MZ-2707) were all obtained from Ningbo Mingzhou Biotechnology Co., Ltd. THLE-2 cellular cultures were grown in 1640 growth medium (R8758, Sigma-Aldrich, USA) comprising 10% FBS, while Huh-7, SNU-182, and JHH7 cells were sustained in DMEM with 10% FBS and 1% penicillin/streptomycin.

CAFs previously incubated with PBS or BMSCs-EVs were seeded in the upper chamber of Transwell co-culture systems (354,480, Corning, USA), with pores measuring 0.4 μm and a cell density of 1×10^5 cells/ml, while the lower enclosure served as the setting for seeding HCC cells. Co-cultivation of CAFs and HCC cells occurred over a period of 24 h prior to the commencement of subsequent experiments involving HCC cells.

Based on experimental requirements, HCC cells co-cultured with CAFs treated differently were divided into the following six groups: PBS, EVs, EVs^{lv-NC}, $EVs^{lv-B4GALT3}$, $EVs^{lv-NC+TNF\alpha}$, and $EVs^{lv-B4GALT3}+TNF\alpha$. In the PBS, EVs, EVs^{lv-NC}, $EVs^{lv-B4GALT3}$, $EVs^{lv-NC}+TNF\alpha$, and $EVs^{lv-B4GALT3}+TNF\alpha$ groups, CAFs were treated with PBS, EVs, EVs^{lv-NC}, $EVs^{lv-B4GALT3}$, $EVs^{lv-NC}+TNF\alpha$, and $EVs^{lv-B4GALT3}+TNF\alpha$, respectively, before co-culturing with HCC cells (Huh-7, SNU-182, or JHH7) (Salah et al. 2022; Zhao et al. 2022).

Construction and grouping of HCC mouse models

The study involved the acquisition of fifty-six vigorous male BALB/c nude mice, aged 4 to 6 weeks, from Charles River, China. Each mouse was accommodated in isolation within SPF-certified animal quarters, with humidity levels set at 60–65% and temperature precisely adjusted to fall between 22 and 25 ℃. Abundant nourishment and hydration were supplied to the mice within a 12-h light–dark rhythm. The experiment initiated after a week of adaptation, with the mice's health being evaluated in advance. The wellbeing of each living organism was ensured in compliance with the guidelines outlined in the "Guide for the Care and Use of Laboratory Animals" published by the National Academy of Sciences and endorsed by the National Institutes of Health. Authorization for the experimental procedures and animal care protocols was provided by the Institutional Animal Ethics Committee (Ethics Approval No: [2022]298).

For the establishment of the orthotopic HCC model, introduction of the orthotopic HCC model involved the injection of 30 μl PBS mixed with 2×10^6 Huh-7 cells into the liver lobes of mice. Starting from the 7th-day post-tumor cell injection, injections were administered to mice intravenously with 100 μl of PBS carrying EVs (10 μg per mouse) or without EVs every second day. After 4 weeks of inoculation, mice were euthanized with 100 mg/kg of pentobarbital sodium (11,715, Merck, USA), and their livers were harvested. THE establishment of the HCC lung metastasis model was accomplished by injecting 2×10^6 Huh-7 cells diluted in 100 μl of PBS into the mice's blood circulation via the tail vein. Starting from the 5th-day post-tumor cell injection, administration of 100 μl of PBS, including EVs (10 μg per rodent), or without EVs, was done through intravenous injection to the mice at four-day intervals. Mice were euthanized 8 weeks post-tumor cell injection, and their lungs were excised. Tumors were dissected to measure the maximum diameter and weight (Jiang et al. 2020; Hou et al. 2020).

Mice were arbitrarily separated into categories in the subsequent manner: Control group (5 mice) and HCC group (51 mice). The Control group received no treatment. The HCC group was further divided into subgroups: HCC group (5 mice), PBS group (3 mice), EVs group (3 mice), HCC + PBS

group (10 mice), HCC + EVs^{lv-NC} group (10 mice), HCC + $EVs^{lv-B4GALT3}$ group (10 mice), and HCC + $EVs^{lv-B4GALT3}$ + TNFα group (10 mice).

In the HCC group, Huh-7 cells were injected to establish an in situ HCC model. In the PBS group and EVs group, after establishing the in situ HCC model, mice received tail vein injections of PBS or BMSCs-EVs respectively. Liver tissues of mice from the Control group, HCC group, PBS group, and EVs group were collected for subsequent transcriptomic sequencing (Jiang et al. 2020; Hou et al. 2020).

For the HCC + PBS group, HCC + EVs^{lv-NC} group, HCC + $EVs^{lv-B4GALT3}$ group, and HCC + $EVs^{lv-B4GALT3}$ + TNFα group, CAFs treated with PBS, EVs^{lv-NC}, $EVs^{lv-B4GALT3}$, or $EVs^{lv-B4GALT3}$ + TNFα were mixed with luciferase-labeled Huh-7 cells in a 1:1 ratio and suspended in PBS, then injected into the liver lobes of mice or tail veins to establish in situ HCC models and lung metastasis HCC models. Five HCC mice from each group were used for in situ or lung metastasis model formation. Following 4 or 8 weeks of model establishment, tumor burden was detected using IVIS Lumina III (PerkinElmer) for bioluminescence imaging. Subsequently, liver or lung tissues were collected from the mice (Jiang et al. 2020; Hou et al. 2020; Liu et al. 2021).

Histological examination

Mouse liver, tumor tissue, and lung tissue were stained using an H&E staining kit (C0105, Beyotime, China). The following are the exact measures taken in progression: the liver and lung samples stemming from the murine models were initially placed in 10% neutral buffered formalin at a temperature of 4 °C for a complete period of 24 h. Following this, they underwent dehydration, were coated with paraffin, and were sliced into individual sections. Xylene was used to deparaffinize the sections, followed by gradual alcohol hydration and rinsing with distilled water. Afterward, the items were immersed in hematoxylin solution for 5–10 min, any extra dye was cleared off with deionized water for about 10 min, and later treated with eosin solution for a period spanning from 30 s to 2 min. Finally, they underwent gradient alcohol dehydration and xylene clearing. Neutral resin or an alternate mounting medium was used to fix the sections, which were then inspected and photographed under an inverted microscope (IX73, Olympus, Japan) (Bai et al. 2022).

TUNEL staining

The TUNEL Kit reagent (C1086, Beyotime, China) was utilized to assess the apoptosis status in mouse tumor tissues. Tissue slices were treated with 3% H_2O_2 and then incubated with 50 μL TUNEL for 60 min, avoiding exposure to light at 37 °C. DAPI staining was applied to the cell nuclei, allowing for a duration of 30 min, after which they were rinsed thrice with PBS. Subsequently, a fluorescence microscope with a camera (BX53, Olympus, Japan) was employed to photograph tumor tissues at a×400 magnification. Calculation of the TUNEL fluorescence area with respect to the DAPI fluorescence area was conducted via the ImageJ application. Every collection was composed of 5 mice, encompassing 5 parts for each mouse randomly viewed in 6–10 territories. ImageJ tool was applied for the assessment of TUNEL-positive cell proportion (Tang et al. 2023).

Immunohistochemistry (IHC) experiment

Tumor tissues were processed through the following steps: fixation in 4% PFA, dehydration, clearing, paraffin embedding, and ultimately sectioning of the tissues. For IHC staining, the sections underwent deparaffinization and rehydration, followed by antigen retrieval. The sections were then immersed in a vessel with PBS and subjected to microwave heating until boiling occurred. Subsequently, immunostaining was carried out applying the universal two-step detection kit (PV-9000, ProteinTech, USA) abiding by the manufacturer's prescribed protocol. The main antibodies utilized were as outlined: Ki67 (12,335–1-AP, 1:500), NF-κB p-p65 (ab131100, 1:100), N-cadherin (ab76011, 1:500), E-cadherin (ab76319, 1:500), and Vimentin (ab92547, 1:500), showing significantly increased expression levels. The utilization of an optical microscope (CX43, OLYMPUS, Japan) facilitated the observation and recording of staining outcomes. Staining in positive regions appeared as light brown or tan hue. Every collection was made up of 5 mice, having 5 segments for every mouse, procured from the matching tissue sample for every mouse. Different protein staining was performed on each Sect. 6–10 fields were randomly selected for observation, and the

amount of positive cells was documented. Inspection was executed utilizing the image interpreting system (Aperio Scanscope System, Vista, CA) (Cai et al. 2021).

HCC Mice liver tissue transcriptomic investigation

Mice in the Control, HCC, PBS, and EVs groups provided liver tissue samples for analysis. The Invitrogen Total RNA Isolation Reagent Kit (12,183,555, USA) was utilized for the isolation and extraction of total RNA from the samples, followed by quantification through OD value assessment. Agarose gel electrophoresis was employed to evaluate the integrity of the total RNA, with a RIN value between 7 and 10 considered high quality. High-quality total RNA underwent reverse transcription to generate cDNA, followed by the assembly of libraries and sequencing conducted on Illumina's NextSeq 500 platform. Initial reads were produced from the sequencing's raw image data by converting them using base calling techniques. Ensuring the superior quality of primary documents, cutadapt was invoked to excise the adapter sequences used for sequencing and eliminate low-quality sequences, resulting in the remaining material designated as "purified reads." After aligning these sequences with the mouse reference genome via the application Hisat2, the quantitative examination of gene expression was performed by employing the R software's limma package, ultimately creating a matrix displaying gene expression levels (Li et al. 2022a, b).

Bioinformatics Analysis

The "limma" software in the R linguistic framework was employed to examine the variations in mRNA expression levels identified in the transcriptome sequencing information. The thresholds applied to differentiate the mRNA distinctions between the Control and HCC samples were determined by |Log2 Fold change| > 2 and P.adj < 0.05. For the PBS and EVs groups, the criteria were set at |Log2 Fold change| > 1 and P.adj < 0.05. Implementation of the ggplot2 software led to the creation of volcano sketches, and the pheatmap package in R facilitated heatmap generation. The Exome Academic Database was employed for the formulation of Venn diagrams (Langfelder and Horvath 2008). The gene set for CAFs was retrieved and downloaded from the GeneCards database (https://www.genecards.org/). The Jaspar database was utilized to predict the binding positions of B4GALT3 with the NF-κB signaling pathway (https://jaspar.genereg.net/). Conducting GO and KEGG pathway assessments in R language was enabled by the integration of "clusterProfiler," "org.Hs.eg.db," "enrichplot," "DOSE," and "ggplot2" packages (Liang et al. 2022, Du et al. 2022).

Immunofluorescent (IF) staining

After fixation in 4% PFA for a quarter of an hour, both cells and tumor tissues underwent dual PBS rinses and were subsequently made penetrable with 0.5% Triton X-100 (P0096, Belltime, China) for 10 min. Later on, both tissues and cells were subjected to overnight incubation at 4 °C with primary antibodies against rabbit anti-α-SMA (ab7817, 1:100), FAP (ab314456, 1:100), NF-κB p-p65 (ab131100, 1:100), B4GALT3 (20,330–1-AP, 1:100), Collagen I (ab270993, 1:100), NF-κB p65 (ab16502, 1:100). Post triple PBS washes, tissue sections were treated with secondary antibodies conjugated with Alexa Fluor 647 (ab150083, 1:200) or Alexa Fluor 488 (ab150077, 1:200) for an hour. Afterward, the segments were rinsed thrice with PBS solution and subjected to staining with DAPI (C1005, Beyotime, 10 μg/mL) for a period of 10 min. The sections were maintained in cold storage at 4 °C and inspected through the use of a fluorescence microscope (IMT-2, Olympus, Japan). For cellular experiments, each cell was evaluated on 5 slices, observing 6–10 fields randomly, repeated 3 times per experiment; for animal experiments, each group consisted of 5 mice, each subjected to 5 slices, with 6–10 fields observed randomly. ImageJ software facilitated the measurement of the fluorescence area of α-SMA, FAP, NF-κB p-p65, and B4GALT3 concerning DAPI fluorescence area, or it was utilized to assess the fluorescence intensity of NF-κB p65 co-localized with DAPI within the cell population. All antibodies were purchased from abcam, except B4GALT3 from Protein tech (Yue et al. 2019).

Dual luciferase reporter gene experiment

From the NCBI database, the protein sequence for B4GALT3 and the DNA sequence of the NF-κB

promoter were extracted and processed for molecular docking analysis using the HDOCK website (http://hdock.phys.hust.edu.cn/). The most stable binding structure was identified as Model_1 (Figure S1A). The pdb file of Model_1 was subsequently uploaded to the PDBsum website (https://www.ebi.ac.uk/thornton-srv/databases/pdbsum/) for further analysis of the binding sequence information between B4GALT3 and the NF-κB promoter DNA (Figure S1B). Co-transfecting BMSCs with lv-NC and lv-B4GALT3 involved the delivery of a fluorescent luciferase reporter plasmid harboring the NF-κB promoter sequence (TATATCTGGC) through the Lipofectamine 2000 reagent kit (11,668,019, Thermo, USA). To serve as an internal control, the cell's luciferase activity post-transfection for 48 h was assessed using the Renilla luciferase assay kit (K801-200, Biovision, USA). Employing the Dual-Luciferase Reporter Assay System from Promega in Madison, WI, USA, allowed for the detection of the luciferase reporter gene. Calculating the ratio between Firefly luciferase assay values (RLU) and Renilla luciferase assay values (RLU) enabled the determination of the activation level of the specific reporter gene (Taniue et al. 2016). Each experiment was repeated thrice for accuracy.

Mutant vectors of dual-luciferase reporter gene constructs

Subsequently, the wild-type NF-κB (NF-κB-WT) site (5'-TATATCTGGC-3') and the mutant NF-κB (NF-κB-MUT) site (5'-CGCGAGTTCC-3') were individually inserted into the pGL-3 luciferase reporter vector (4,351,372, Thermo Fisher, USA). The co-transfection of NF-κB-WT and NF-κB-MUT luciferase reporter plasmids with lentiviral vectors carrying lv-NC and lv-B4GALT3 into CAFs was followed by cell retrieval and lysis after 48 h. The supernatant, derived post-centrifugation at 250 × g for 3–5 min, was integrated with the Dual-Luciferase® Reporter Assay System (E1910a, Promega, USA) for the evaluation of luciferase performance. Treatment of individual cell samples involved the application of 100 µL of Firefly Luciferase working solution for Firefly Luciferase detection and 100 µL of Renilla Luciferase working solution for Renilla Luciferase detection, comparing the relative luciferase activity of Firefly to Renilla Luciferase (Jin et al. 2020). Each experiment was repeated thrice.

Scratching experiment

In the cell scratching experiment, the 6-well plate received HCC cells at full seeding density. The cell layer was scratched using the tip of a sterile pipette (200 µL) and then gently washed with PBS solution three times. Cell observation and photography were conducted at 0, 24, and 48 h intervals to analyze the healing area of the scratch in each group. Before the scratching study, cells were treated with cytochalasin D (1 µg/mL, M5353, Sigma-Aldrich) for 1 h to eliminate any cell proliferation defects. The scratch's width was gauged initially (T = 0 h) and subsequently at 24 h (T = 24 h) and 48 h (T = 48 h). Cell migration ability was evaluated by calculating the difference in scratch width between the two time points and expressed as a percentage. Five images were taken for each cell, and inspections took place in 6–10 fields of sight that were chosen randomly (Song et al. 2015). Thrice the test was replicated for validation purposes.

Transwell experiment

Two types of cell culture inserts were utilized in the Transwell experiment: Application of Transwell PC filter cell incubation equipment (CLS3422, Corning, USA) and BioCoat Matrigel infiltration assemblies employing 8.0 µm PET layer (354,480, Corning, USA). Co-cultured HCC cells with CAFs were seeded at 1×10^4 cells in the upper chamber with or without matrix gel, followed by adding DMEM containing 10% FBS to the lower chamber. After incubation for 24 h post-seeding, cells underwent fixation with 4% PFA followed by a gentle removal from the upper polycarbonate membrane employing a cotton swab. A crystal violet stain solution (C0121, Beyotime, China) was used to color cells that underwent migration and invasion. Examination under an inverted microscope (XDS-900, Caikon, China) revealed five partitions per cell in 6–10 randomly selected fields. The "Analyze Particles" feature in ImageJ was employed to quantify the invading cell numbers in every single image (Mao et al. 2021a, b). The validation process included three separate repetitions for every experiment.

Detection of cell apoptosis by flow cytometry

The dual staining approach utilizing Annexin V-FITC and propidium iodide (PI) was employed to analyze cellular apoptosis in Huh-7 cells. 2×10^5 cells of the Huh-7 cell line were placed in each well of a 6-well plate and exposed to trypsin (R001100, Gibco, USA). Retrieval of the supernatant was achieved through centrifugation of cells at 800 g in 15 mL centrifuge tubes. Suspension of the pellet took place in 500 µL of binding buffer, followed by a 15-min incubation period with 5 µL of FITC and 5 µL of PI in a darkened environment, in line with the protocols specified by the apoptosis detection kit (556,547, BD Biosciences, USA). A flow cytometer obtained from BD Biosciences in the USA was employed to analyze apoptosis in the cell suspension. Necrotic cells were observed in the quadrant positioned at the top left, late apoptotic cells in the quadrant positioned at the top right, early apoptotic cells in the quadrant positioned at the bottom right, and normal cells in the quadrant positioned at the bottom left. The calculation of the apoptosis rate involved summing the percentages of cells in the upper right and lower right quadrants (Zuo et al. 2022). Every trial was repeated on three occasions.

RT-qPCR

Isolation of total RNA from cellular populations and tumor samples was performed applying TRIzol (15,596,026, ThermoFisher, USA), followed by the determination of its concentration and purity employing a nanodrop2000 spectrophotometer (ThermoFisher, USA). The extracted RNA was reverse-transcribed to cDNA following the instructions of the PrimeScript RT reagent Kit (RR047A, Takara, Japan) and then subjected to RT-PCR applying the Fast SYBR Green PCR Master Mix (11,736,059, ThermoFisher, USA). The internal control chosen was GAPDH, with triplicate setups for each well. Assessment of gene expression levels was done employing the $2^{-\Delta\Delta Ct}$ technique, and the trial was reiterated three times. Table S3 contains the primer sequences applied for RT-qPCR in this investigation (Liang et al. 2017).

WB

Lysis of cells and tumor tissues was conducted in RIPA lysis buffer (P0013B, Beyotime Biotechnology, China), with the quantification of protein concentrations accomplished using the BCA method (A53226, Thermo Fisher Scientific, USA). Separation of the proteins was carried out via polyacrylamide gel electrophoresis, and subsequently, they were transferred onto a PVDF membrane (PVH85R, Millipore, Germany) applying a wet transfer method. Blocking of the membrane occurred using 5% BSA for an hour at room temperature, followed by an incubation overnight at 4 °C with the primary antibodies mentioned: rabbit anti-α-SMA (ab7817, 1:1000), FAP (ab314456, 1:1000), B4GALT3 (20,330–1-AP, 1:1000), rabbit anti-Collagen I (ab316222, 1:1000), rabbit anti-p-IκBα (2859, 1:1000), rabbit anti-IκBα (4812, 1:1000), rabbit anti-NF-κB p65 (ab32536, 1:1000), rabbit anti-NF-κB p-p65 (ab131100, 1:1000), and rabbit anti-GAPDH (ab8245, 1:1000). The cleansing of the membrane was followed by incubation with a secondary antibody that was conjugated with HRP-goat anti-rabbit IgG (ab6721, at a concentration of 1:5000) for up to 2 h. Three 5-min cycles of TBST washings were conducted on the membrane. The identification of proteins was executed employing a chemiluminescent imaging device, and the evaluation of protein quantities was carried out utilizing ImageJ software, assessing the protein expression levels against the grayscale proportion of the loading control GAPDH or the corresponding non-phosphorylated protein. Every test underwent replication on three occasions. Notably, B4GALT3 was procured from Protein tech, p-IκBα and IκBα were obtained from Cell Signaling Technology, and all other antibodies were purchased from Abcam (Zou et al. 2016).

Statistical analysis in research

Utilization of SPSS software (version 21.0, IBM, USA) facilitated the statistical analysis of data in this study, presenting all data as mean ± standard deviation (mean ± SD). All significance tests were two-tailed. Initially, the normal distribution was assessed using the Kolmogorov–Smirnov test. Assuming normal data distribution, two groups were compared using unpaired t-tests, with multiple group comparisons conducted through one-way ANOVA or repeated

measures ANOVA. The Wilcoxon signed-rank test was utilized to examine significant disparities between the dual groups for data that was not distributed normally. Significance in statistics was denoted by a p-value lower than 0.05 (Wan et al. 2023; Xu et al. 2022).

Results

Identification of Potential Targets Regulating HCC Progression through Screening EVs with Transcriptome Sequencing Data.

To further demonstrate the impact of CAFs on HCC progression, it is essential to establish a HCC nude mouse model, as illustrated in Figure S2A. Additionally, tissue sections underwent histological analysis, with staining using hematoxylin and eosin indicating normal liver histology in the control group mice, devoid of inflammation or cellular infiltration. Conversely, the liver tissue sections of the HCC group mice exhibited visible infiltration of tumor cells, enlarged and deeply stained nuclei, and closely packed tumor cells, indicating successful modeling (Figure S2B). External images of the tumors, along with measurements of their maximum diameter and weight, demonstrated that relative to the control group, the livers of the HCC group mice appeared tan-yellow with evident tumors, and the tumors demonstrated a substantial enlargement in both diameter and mass (Figure S2C).

Subsequently, transcriptome sequencing was performed on the liver tissues of mice in the Control and HCC groups (Fig. 1A). Differential analysis was conducted using a cutoff of $|\text{Log2 Fold change}| > 2$ and $\text{P.adj} < 0.05$, revealing the presence of 250 differentially expressed genes (DEGs) between the liver tissues of the HCC and Control groups, with 108 upregulated and 142 downregulated genes (Fig. 1B-C). Detailed information can be found in Table S4. To further identify characteristic genes of HCC, DEGs were screened using the Lasso and SVM-RFE machine learning algorithms. B4GALT3, PLCD3, SGK2, and AVPR1A were singled out as feature genes by the Lasso technique (Fig. 1D), while the SVM-RFE algorithm has revealed 4 genes of interest: B4GALT3, TNFRSF12A, ANKRD1, and AQP9 (Fig. 1E). The genes obtained from these two machine learning algorithms were intersected with the CAFs dataset from the GeneCards database, resulting in the identification of CAFs-relevant key feature gene B4GALT3 (Fig. 1F). In the transcriptome sequencing data, the expression of B4GALT3 was found to be downregulated in the HCC group (Fig. 1G).

Subsequently, BMSCs were isolated and characterized. Inverted microscopy revealed that BMSCs reached 80% confluence and exhibited a spindle shape in the 3rd generation (P3). The presence of red calcified nodules and lipid droplets in BMSCs, as revealed by Safranin O and Oil Red O staining, serves as evidence of their competence in osteogenic and adipogenic differentiation (Figure S3A). Flow cytometry analysis showed that BMSCs were positive for CD90 (25–35 kDa GPI-anchored protein, a BMSC marker) and CD73 (69 kDa GPI-anchored protein, a BMSC marker) but negative for CD45 (a hematopoietic stem cell marker), indicating the absence of hematopoietic stem cells in BMSCs (Figure S3B). These results confirmed the successful isolation of BMSCs. BMSCs-EVs were obtained through ultracentrifugation and assessed by TEM, NTA, and WB. TEM analysis revealed that EVs were elliptical with uniform size (Figure S3C). NTA data showed an average EV diameter of 99.3 ± 2.1 nm and a concentration of 1.5×10^6 particles/mL (Figure S3D). WB analysis indicated strong expression of transmembrane proteins CD9 and CD63, as well as intracellular proteins TSG101 and HSP70, while the endoplasmic reticulum marker Calnexin was not detected (Figure S3E). These results confirmed the successful extraction of BMSCs-EVs.

To further evaluate the impact of BMSCs-EVs on HCC, we treated HCC mice with either PBS or BMSCs-EVs and collected mouse liver for analysis (Fig. 2A). Contrasted against the PBS group, mice in the EVs group exhibited a significant decrease in the maximum diameter and weight of tumors in the liver (Fig. 2B). Additionally, H&E staining results revealed that in the liver sections of mice from the PBS group, tumor cell infiltration, enlarged tumor cell nuclei, intense staining, and dense arrangement of tumor cells were evident. Conversely, contrasted with the mice in the PBS group, tumor cell infiltration notably decreased in the liver sections of mice in the EVs group (Fig. 2C). Subsequently, transcriptome sequencing was conducted on the livers of HCC mice in both the EVs and PBS groups, with a threshold of $|\text{Log2 Fold change}| > 2$ and $\text{P.adj} < 0.05$ set for

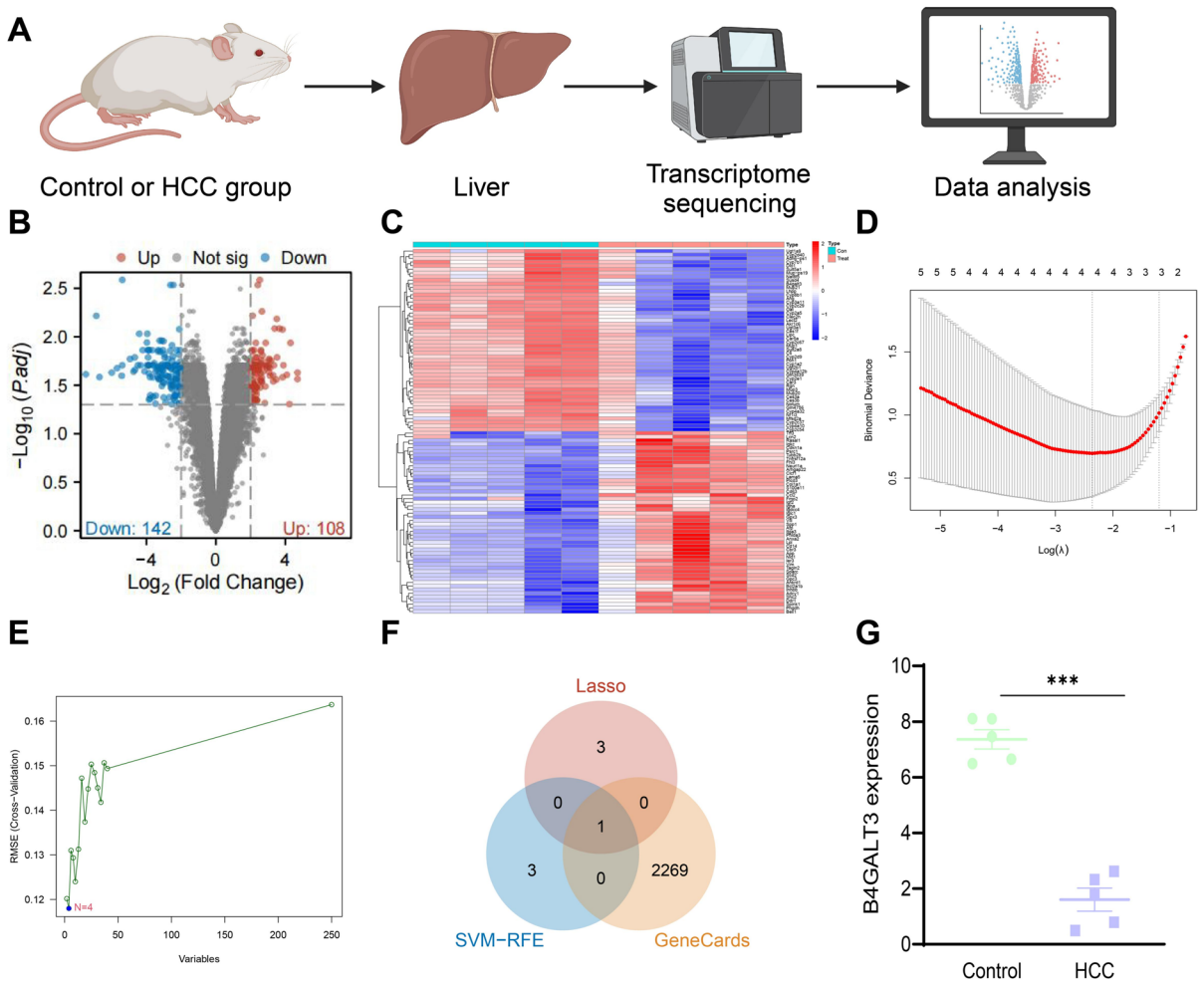

Fig. 1 Analysis of DEGs in the Transcriptome of Control and HCC Mice and Their Correlation with CAFs in HCC, Showing Decreased Expression of B4GALT3, Implying Its Potential Key Role in Regulating the TME. Note: (**A**) Schematic diagram of transcriptome sequencing; (**B**) Volcano plot of DEGs between the liver tissues of Control group (n = 5) and HCC group (n = 5) mice; (**C**) Heatmap of DEGs between the liver tissues of Control group (n = 5) and HCC group (n = 5) mice; (**D**) Identification of 4 characteristic genes in HCC using the LASSO algorithm; (**E**) Identification of 4 characteristic genes in HCC using the SVM-RFE algorithm; (**F**) Venn diagram showing the intersection of results from LASSO and SVM-RFE machine learning algorithms with CAFs gene data from the GeneCards database; (**G**) Expression levels of B4GALT3 in the transcriptome sequencing data of the liver tissues of Control group (n = 5) and HCC group (n = 5) mice; values are presented as mean ± standard deviation, *** indicates $P < 0.001$

differential analysis. The findings indicated that the liver tissue of mice in the EVs group exhibited 648 downregulated differentially expressed genes and 965 upregulated differentially expressed genes compared to the PBS group (Fig. 2D). Notably, HCC mice in the EVs group showed upregulated B4GALT3 expression within their liver tissue (Fig. 2E).

Subsequently, enrichment assessment was implemented on the DEGs. The outcomes of the GO analysis revealed a predominant enrichment of the DEGs in biological processes (BP) such as leukocyte migration, negative regulation of immune system process, positive regulation of cell adhesion, and regulation of cell–cell adhesion. Concerning cellular components (CC), the DEGs were mainly enriched in the collagen-containing extracellular matrix, receptor complex, membrane rafts on the cell membrane, and membrane microdomains. In relation to molecular

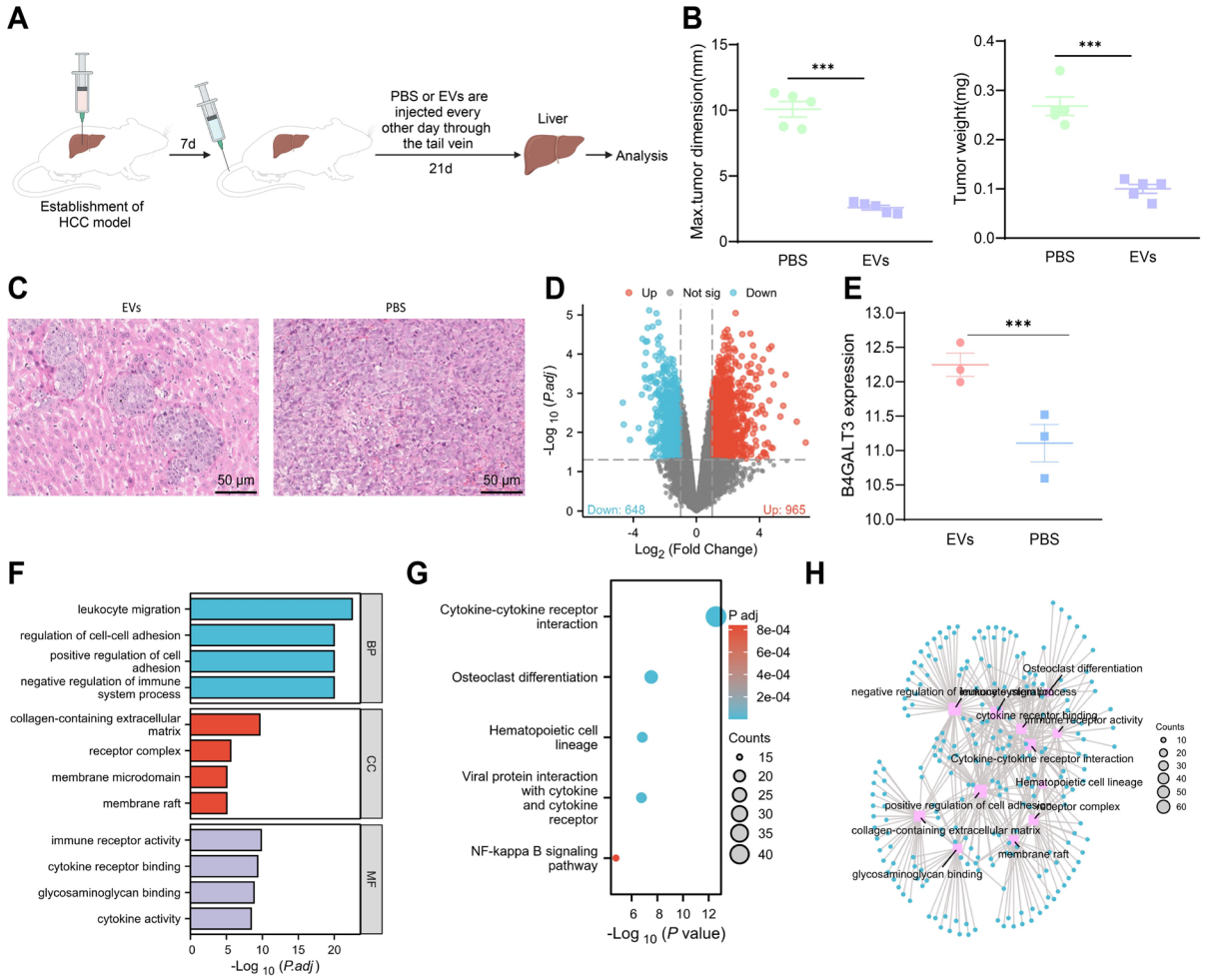

Fig. 2 Effects of BMSCs-EVs on HCC Mice and Transcriptome Sequencing Bioinformatics Analysis. Note: (**A**) Schematic representation of in situ HCC mice treated with PBS or EVs; (**B**) Gross view of liver and quantitative analysis of tumor maximum diameter and weight after tumor resection in in situ HCC mice treated with PBS (n = 3) or EVs (n = 3); (**C**) Representative images of liver cell morphology and structure in in situ HCC mice (n = 3) stained with H&E, scale bar = 50 μm; (**D**) Volcano plot of DEGs in liver transcriptome sequencing of in situ HCC mice treated with PBS (n = 3) or EVs (n = 3); (**E**) Expression of B4GALT3 in liver transcriptome sequencing data of in situ HCC mice in each group; (**F**) Bar graph of GO enrichment analysis of DEGs between liver samples of in situ HCC mice (n = 3) in each group in transcriptome sequencing; (**G**) Bubble chart of KEGG enrichment analysis of DEGs between liver samples of in situ HCC mice (n = 3) in each group in transcriptome sequencing; (**H**) Network diagram of GO and KEGG enrichment analysis of DEGs between liver samples of in situ HCC mice (n = 3) in each group in transcriptome sequencing. The values are presented as mean ± standard deviation, *** indicates $P < 0.001$

function (MF), the DEGs exhibited significant enrichment in immune receptor activity, cytokine receptor binding, galectin binding, and cytokine activity (Fig. 2F). These findings are closely related to exosome secretion and tumor immunity. According to the KEGG examination, the DEGs displayed notable enrichments in pathways such as cytokine-cytokine receptor interaction, osteoclast differentiation signaling pathway, hematopoietic cell lineage signaling pathway, viral protein interaction with cytokine and cytokine receptor signaling pathway, and NF-κB signaling pathway, where NF-κB pathway emerged as the most remarkable one (Fig. 2G). The network diagram of the enrichment analysis is presented in Fig. 2H. Numerous academic works have illustrated the induction of the NF-κB signaling pathway in

HCC (Xu et al. 2021). Therefore, we hypothesize that EVs may influence the NF-κB signaling pathway by delivering B4GALT3, thereby inhibiting the progression of HCC.

BMSCs-EVs deliver B4GALT3 to inhibit CAFs' activity

Based on bioinformatics analysis and experimental results, we propose that BMSCs-EVs inhibit the progression of HCC by upregulating B4GALT3. CAFs represent one of the most abundant components in the TME of HCC and are closely associated with its development (Xu et al. 2022). Therefore, to investigate whether BMSCs-EVs can modulate CAFs through B4GALT3 to treat HCC, we co-cultured CAFs with BMSCs-EVs for 24 h. The Dil staining revealed that CAFs could uptake BMSCs-EVs (Fig. 3A). WB analysis showed that EVs exhibited higher expression levels of B4GALT3 compared to BMSCs (Fig. 3B), indicating the enrichment of B4GALT3 in EVs. Subsequently, treating CAFs with PBS or EVs, WB and IF staining demonstrated that in the CAFs + EVs group, the B4GALT3 expression in CAFs showed an augment post BMSCs-EVs intervention (Fig. 3C-D), suggesting the ability of BMSCs-EVs to deliver B4GALT3 to CAFs.

To further validate whether BMSCs-EVs modulate the functionality of CAFs by delivering B4GALT3, we initially co-cultured PBS or EVs with CAFs and observed the impact of EVs on the activity of CAFs. WB and IF staining indicated that EVs treatment reduced the expression of activated fibroblast markers α-SMA and FAP in CAFs (Figure S4A-C). Additionally, CCK8 results demonstrated that EVs treatment inhibited the cell viability of CAFs (Figure S4D), implying that BMSCs-EVs potentially suppress CAFs' activity by delivering B4GALT3.

Furthermore, studies have shown that activated CAFs remodel the TME by depositing collagen proteins, thereby supporting the advancement of HCC (Sun et al. 2023). Subsequently, the variations in Collagen I levels in CAFs upon EVs treatment were investigated using WB and IF assessment. The results revealed downregulation of Collagen I expression by EVs (Figure S4E-F), indicating that inhibiting the activation of CAFs can suppress the deposition of collagen proteins, further supporting the potential impact of CAFs in the TME on HCC.

To further validate whether BMSCs-EVs suppress CAF activity through the delivery of B4GALT3, we constructed lentiviral vectors and verified their knockdown efficiency through RT-qPCR, selecting the sh-B4GALT3-1 with the highest knockdown efficiency for further investigations (Fig. 3E). Immunostaining outcomes revealed that, in contrast with the lv-NC group, B4GALT3 was notably amplified in BMSCs of the lv-B4GALT3 group; and in relation to the sh-NC group, B4GALT3 was substantially lowered in BMSCs of the sh-B4GALT3 group (Fig. 3F).

Next, we isolated BMSCs-EVs with B4GALT3 overexpression and silencing and co-cultured these EVs with CAFs. WB and IF outcomes revealed that in contrast with EVs^{lv-NC} group, B4GALT3 expression was increased in CAFs exposed to $EVs^{lv-B4GALT3}$ group, with decreased expression of the activation markers α-SMA and FAP. Conversely, when comparing EVs^{sh-NC} group, CAFs treated with $EVs^{sh-B4GALT3}$ group exhibited reduced B4GALT3 expression alongside increased levels of α-SMA and FAP (Fig. 3G-I). CCK8 assay data indicated a notable drop in cell viability of CAFs treated with $EVs^{lv-B4GALT3}$ group relative to the lv-NC group, while there was a marked growth in cell viability of CAFs treated with $EVs^{sh-B4GALT3}$ group contrasted against the sh-NC group (Fig. 3J). Furthermore, WB examination displayed a decline in Collagen I expression in CAFs treated with $EVs^{lv-B4GALT3}$ group and an escalation in Collagen I expression in CAFs treated with $EVs^{sh-B4GALT3}$ group (Fig. 3K).

In conclusion, the transfer of B4GALT3 via BMSCs-EVs suppresses CAFs activity, which may impact HCC progression through inhibiting collagen deposition.

Delivery of BMSCs-EVs Suppresses CAFs Activity by Inhibiting NF-κB Signaling Pathway Activation Through B4GALT3.

In line with previous bioinformatics analysis, B4GALT3 was found to be highly expressed in EVs-treated HCC mice and linked to the NF-κB signaling pathway within EVs. To confirm if BMSCs-EVs transferring B4GALT3 inhibits CAF activity via the NF-κB signaling pathway, we initially conducted dual-luciferase reporter gene assays and WB experiments to investigate the relationship between B4GALT3 and the NF-κB signaling pathway, with the binding sites of B4GALT3 and NF-κB shown in Figure S1. The findings yielded from the dual-luciferase

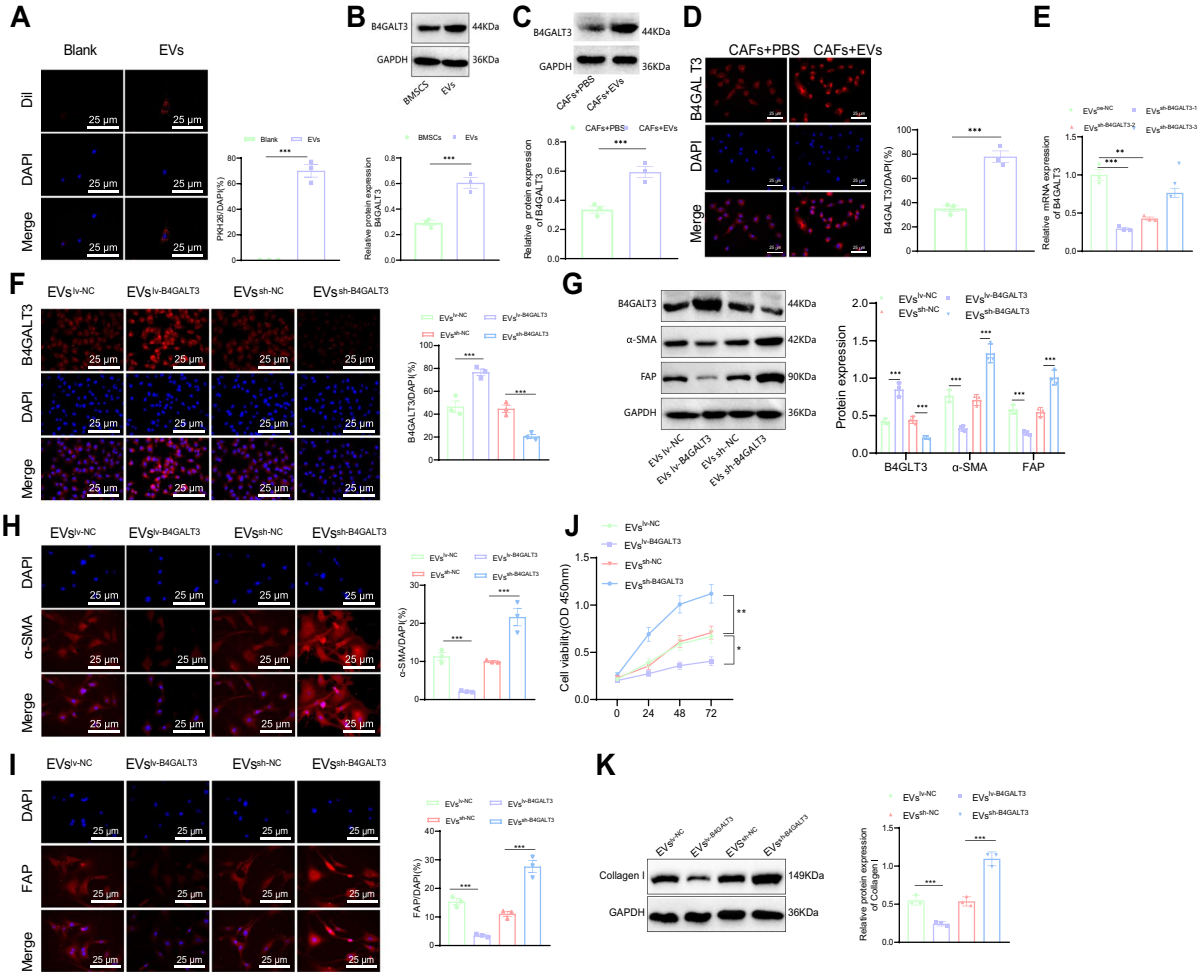

Fig. 3 Impact of BMSCs-EVs Delivery of B4GALT3 on CAFs Viability and Collagen I Expression. Note: (**A**) Dil staining to detect the uptake of EVs by CAFs, scale bar = 25 μm; (**B**) WB analysis of B3GALT3 expression in BMSCs and EVs; (**C**) WB analysis of B4GALT3 protein expression in CAFs treated with PBS or EVs; (**D**) IF staining for B4GALT3 protein expression in CAFs treated with PBS or EVs; (**E**) RT-qPCR analysis of B4GALT3 expression in BMSCs overexpressing (lv-B4GALT3) or silencing (sh-B4GALT3) B4GALT3; (**F**) IF staining to examine B4GALT3 expression in BMSCs, scale bar = 25 μm; (**G**) WB analysis of B4GALT3, α-SMA, and FAP expression in CAFs treated with different EVs; (**H**) IF staining to assess α-SMA expression in CAFs treated with different EVs, scale bar = 25 μm; (**I**) IF staining to evaluate FAP expression in CAFs treated with different EVs, scale bar = 25 μm; (**J**) CCK-8 assay to measure the cell viability of CAFs in each group; (K) WB analysis of Collagen I expression in CAFs treated with different EVs. All experiments were repeated three times, and values are presented as mean ± standard deviation. * denotes $P < 0.05$; ** denotes $P < 0.01$; *** denotes $P < 0.001$

reporter gene mutant vector investigation demonstrated a substantial reduction in luciferase activity in the lv-B4GALT3 group relative to the lv-NC group in the NF-κB-WT group, while no noteworthy alteration was observed in the corresponding NF-κB-MUT group (Fig. 4A), indicating a direct interaction between B4GALT3 and NF-κB.

Furthermore, to further explore whether B4GALT3 mediates the initiation of the NF-κB pathway in regulating CAFs, we treated CAFs with EVs with or without the NF-κB activator Diprovocim (TNFα). WB results indicated a substantial upregulation of B4GALT3 in CAFs in the $EVs^{lv-B4GALT3}$ group in contrast with the EVs^{lv-NC} group, and a

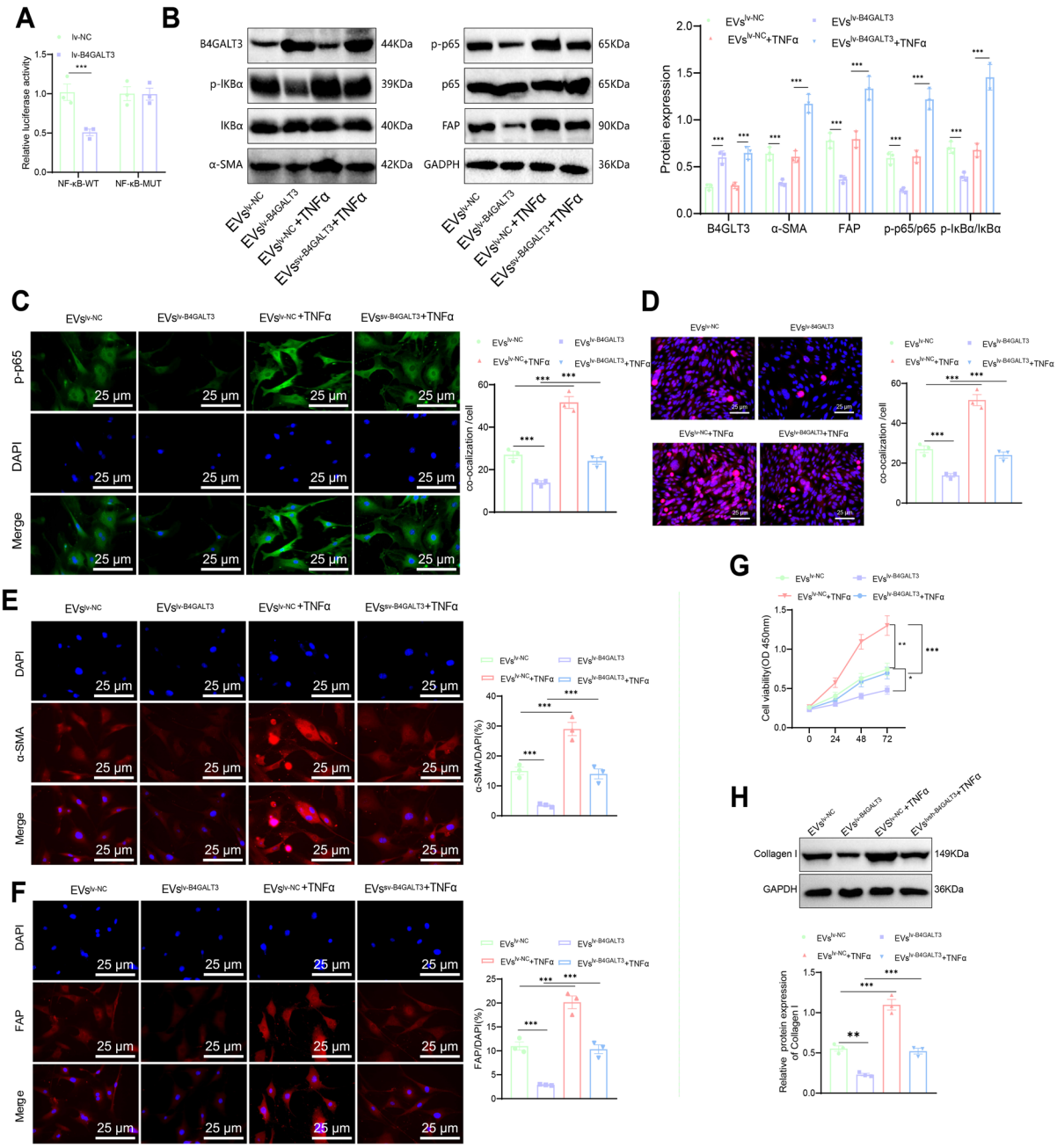

Fig. 4 Impact of BMSCs-EVs Overexpressing B4GALT3 on the Activity of CAFs via the NF-κB Signaling Pathway. Note: (**A**) Dual-Luciferase Reporter Gene Assay to investigate the relationship between B4GALT3 and NF-κB; (**B**) WB analysis of B4GALT3, α-SMA, FAP, p-IκBα, IκBα, p-p65, and p65 expression in CAFs; (**C**) IF staining for p-p65 in CAFs of each group, scale bar = 25 μm; (**D**) IF staining for p65 in CAFs of each group (scale bar = 25 μm), fluorescence intensity of p65 co-localized with the cell nucleus in each cell, p65 (red), DAPI (cell nucleus, blue); (**E**) IF staining for α-SMA in CAFs of each group, scale bar = 25 μm; (**F**) IF staining for FAP in CAFs of each group, scale bar = 25 μm; (**G**) CCK-8 assay to evaluate the cell viability of CAFs in each group; (H) WB analysis of Collagen I expression in CAFs of each group. All experiments were repeated three times, and values are presented as mean ± standard deviation, * indicates $P < 0.05$, ** indicates $P < 0.01$, *** indicates $P < 0.001$

significant downregulation of the activation markers α-SMA and FAP, and the expression of NF-κB signaling pathway proteins p-IκBα/IκBα and p-p65/p65. In the EVs^{lv-NC} + TNFα group, no remarkable shift was identified in the expression of B4GALT3 among CAFs, but there was a noteworthy surge in α-SMA, FAP, p-IκBα/IκBα, and p-p65/p65 levels. When contrasted with the $EVs^{lv-B4GALT3}$ group, the $EVs^{lv-B4GALT3}$ + TNFα group exhibited no alteration in B4GALT3 expression in CAFs, but a marked growth in α-SMA, FAP, p-IκBα/IκBα, and p-p65/p65 expression (Fig. 4B). These findings elucidate that BMSCs-EVs may inhibit CAFs activity by delivering B4GALT3 to suppress NF-κB signaling pathway activation.

Subsequently, we conducted IF staining for p-p65 and p65, and the observations revealed that, contrasted against the EVs^{lv-NC} group, the level of p-p65 and the nuclear translocation of p65 in CAFs were substantially lowered in the $EVs^{lv-B4GALT3}$ group. In contrast, in the EVs^{lv-NC} + TNFα group, the expression of p-p65 and the nuclear translocation of p65 were considerably escalated. Furthermore, in relation to the $EVs^{lv-B4GALT3}$ group, the $EVs^{lv-B4GALT3}$ + TNFα group exhibited a significant increase in the expression of p-p65 and the nuclear translocation of p65 (Fig. 4C-D). These findings further confirm that BMSCs-EVs inhibit the activation of the NF-κB signaling pathway by delivering B4GALT3.

Subsequent experiments were conducted to verify the impact of the B4GALT3/NF-κB pathway mediated by BMSCs-EVs on CAFs activity. IF staining outcomes displayed that, in contrast with the EVs^{lv-NC} group, the fluorescence intensity of α-SMA and FAP in CAFs was substantially reduced in the $EVs^{lv-B4GALT3}$ group. Conversely, in the EVs^{lv-NC} + TNFα group, the fluorescence intensity of α-SMA and FAP showed a marked increase. Moreover, contrasted against the $EVs^{lv-B4GALT3}$ group, the $EVs^{lv-B4GALT3}$ + TNFα group illustrated a noteworthy surge in the fluorescence intensity of α-SMA and FAP (Fig. 4E-F). CCK8 assays indicated that, relative to the EVs^{lv-NC} group, the cellular activity of CAFs was noticeably lessened in the $EVs^{lv-B4GALT3}$ group, whereas it was markedly enhanced in the EVs^{lv-NC} + TNFα group. Furthermore, when juxtaposed with the $EVs^{lv-B4GALT3}$ group, the $EVs^{lv-B4GALT3}$ + TNFα group showed a notable increase in CAFs cellular activity (Fig. 4G). Moreover, relative to the EVs^{lv-NC} group, the downregulation of Collagen I expression was observed in CAFs of the $EVs^{lv-B4GALT3}$ group, which was significantly upregulated upon TNFα treatment; similarly, as opposed to the EVs^{lv-NC} group, there was a remarkable upsurge in the expression of Collagen I in CAFs of the EVs^{lv-NC} + TNFα group (Fig. 4H). These results provide further validation for our conclusions.

Overall, these results demonstrate that BMSCs-EVs delivering B4GALT3 prevent the initiation of the NF-κB signaling pathway, thereby inhibiting the activity of CAFs.

BMSCs-EVs Suppress Migration and Invasion of HCC Cells while Inducing Apoptosis.

Delving into the impact of BMSCs-EVs on the malignant phenotype of HCC cells through the modulation of CAFs' activity, we co-cultured EVs-treated CAFs with HCC cells following PBS or EVs treatment (Figure S5A). Results from scratch and Transwell assays indicated that, in relation to the PBS group, co-culture of EVs-treated CAFs with HCC cells (Huh-7, SNU-182, and JHH7) significantly inhibited the migration and invasion of HCC cells (Figure S5B-D). Conversely, EVs-treated CAFs notably promoted apoptosis in Huh-7, SNU-182, and JHH7 cells (Figure S5E). These findings suggest that BMSCs-EVs delivering B4GALT3 suppress CAFs' activity, thereby reducing the migratory and invasive capabilities of HCC cells and promoting their apoptosis, ultimately ameliorating the aggressive phenotype of HCC.

To further validate this conclusion, we co-cultured CAFs treated with EVs^{lv-NC}, $EVs^{lv-B4GALT3}$, EVs^{lv-NC} + TNFα, and $EVs^{lv-B4GALT3}$ + TNFα with HCC cells (Fig. 5A, Figure S6A). Cell scratch and Transwell experiments revealed that, in contrast with the EVs^{lv-NC} group, the migration and invasion of Huh-7, SNU-182, and JHH7 cells were significantly reduced in the $EVs^{lv-B4GALT3}$ group. Moreover, the addition of TNFα to the EVs^{lv-NC} group or $EVs^{lv-B4GALT3}$ group markedly heightened the migratory and invasive behavior of HCC cells (Fig. 5B-D, Figure S6B-D). Furthermore, flow cytometry experiments showed a marked growth in apoptosis in HCC cells in the $EVs^{lv-B4GALT3}$ group

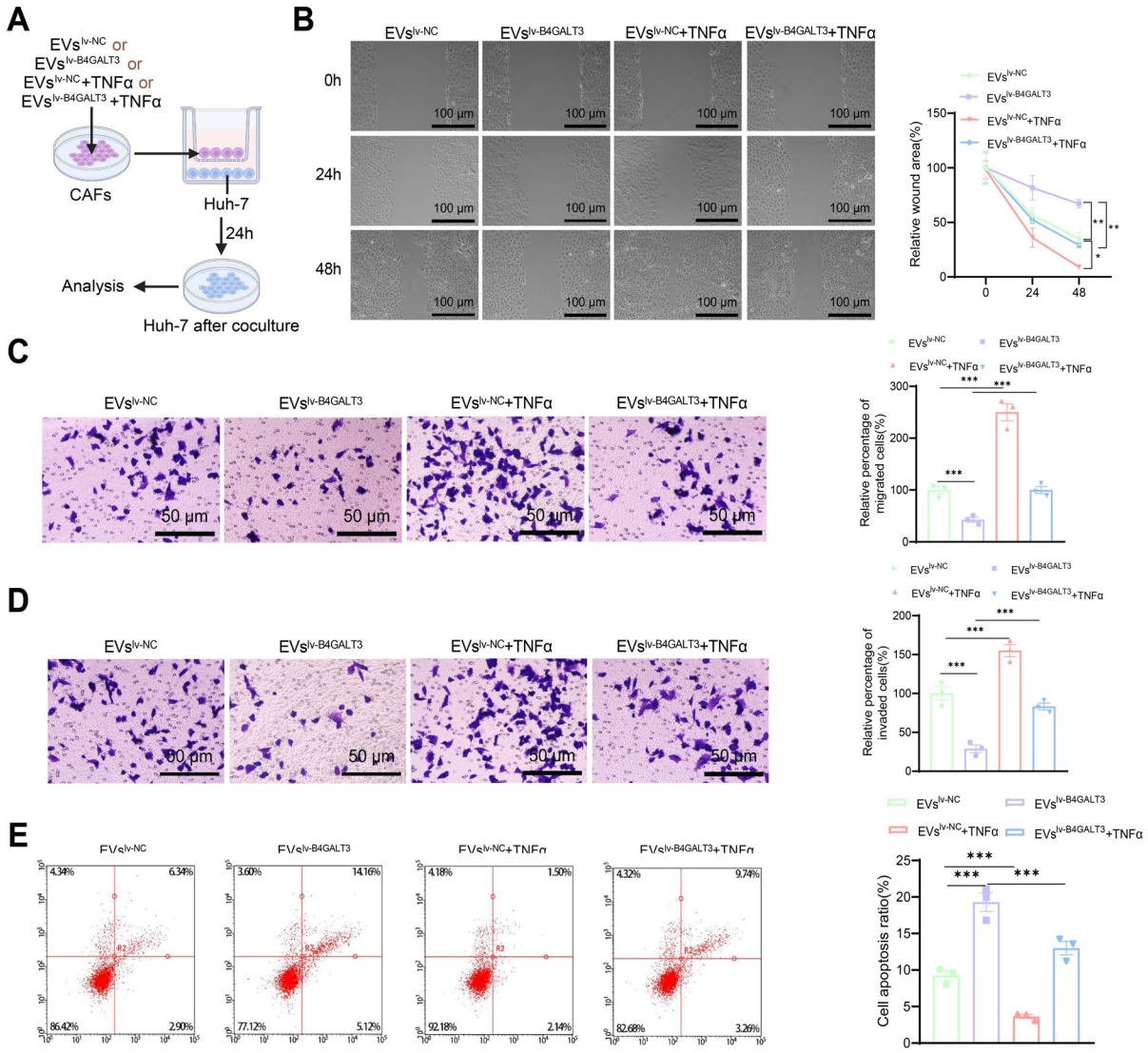

Fig. 5 Impact of Various Treatments of CAFs on the Malignant Phenotype of Huh-7 Cells. Note: (**A**) Schematic representation of the co-culture of Huh-7 cells with different treated CAFs; (**B**) Wound healing assay evaluating the migration ability of HCC cells in each group, scale bar = 100 μm; (**C**) Transwell assay assessing the migration of HCC cells in different groups, scale bar = 50 μm; (**D**) Transwell assay assessing the invasion of HCC cells in different groups, scale bar = 50 μm; (**E**) Flow cytometry measuring the apoptosis of HCC cells in different groups; All experiments were repeated thrice, and values are presented as mean ± standard deviation. * indicates $P < 0.05$, ** indicates $P < 0.01$, *** indicates $P < 0.001$

relative to the EVs^{lv-NC} group; the administration of TNFα to the EVs^{lv-NC} group resulted in a notable drop in HCC cell apoptosis (Figure S6E). Additionally, HCC cell apoptosis was notably reduced in the $EVs^{lv-B4GALT3}+TNFα$ group in contrast with the $EVs^{lv-B4GALT3}$ group (Fig. 5E).

To sum up, the inhibition of CAF activation by BMSCs-EVs through the B4GALT3/NF-κB pathway results in the suppression of HCC cells'

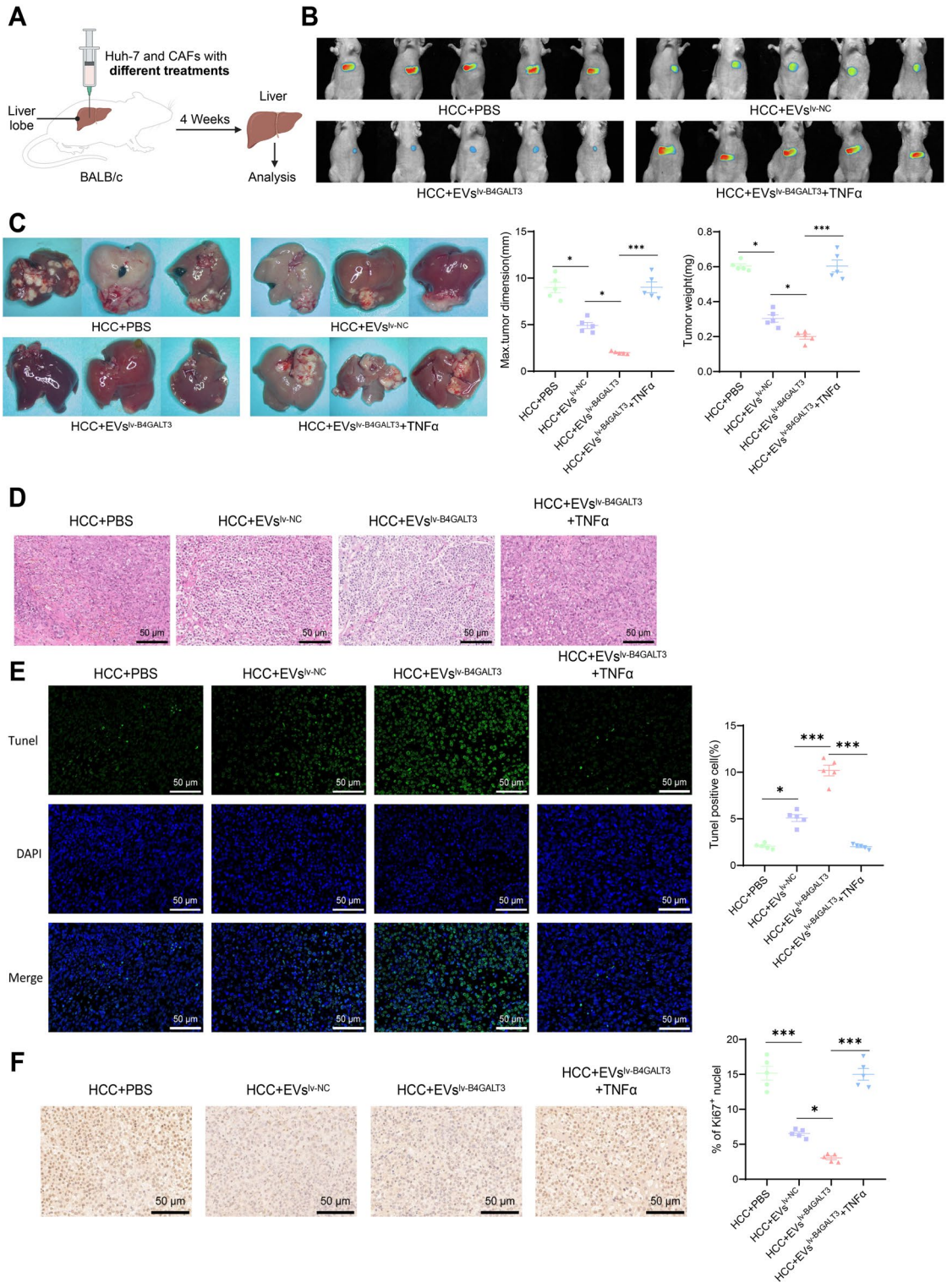
A
Huh-7 and CAFs with different treatments
Liver lobe
4 Weeks
Liver
Analysis
BALB/c
B
HCC+PBS
HCC+EVslv-NC
HCC+EVslv-B4GALT3
HCC+EVslv-B4GALT3+TNFα
C
HCC+PBS
HCC+EVslv-NC
HCC+EVslv-B4GALT3
HCC+EVslv-B4GALT3+TNFα
Max.tumor dimension(mm)
Tumor weight(mg)
D
HCC+PBS
HCC+EVslv-NC
HCC+EVslv-B4GALT3
HCC+EVslv-B4GALT3 +TNFα
50 μm
E
Tunel
DAPI
Merge
Tunel positive cell(%)
F
% of Ki67+ nuclei

◂**Fig. 6** Impact of Different Treatments of CAFs on the Growth of HCC in Mice. Note: (**A**) Schematic representation of the in situ HCC model co-injected with CAFs subjected to different treatments and Huh-7 cells; (**B**) In vivo bioluminescence imaging monitoring tumor growth in each group of mice (n = 5); (**C**) Gross appearance of livers and quantitative assessment of tumor size and weight after tumor resection in each group of mice (n = 5); (**D**) Representative images of tumor tissue morphology and structure in each group of mice (n = 5) assessed by H&E staining, scale bar = 50 μm; (**E**) Representative images of tumor tissue cell apoptosis detected by Tunel staining in each group of mice (n = 5), with quantitative analysis of Tunel-positive cell percentage, scale bar = 50 μm; (**F**) IHC analysis of Ki67 expression in tumor tissue of each group of mice (n = 5), scale bar = 50 μm. Values are presented as mean ± standard deviation, * indicates $P < 0.05$, ** indicates $P < 0.01$, *** indicates $P < 0.001$

migration and invasion abilities while fostering their apoptotic processes.

BMSCs-EVs-B4GALT3 Inhibit HCC tumor growth and metastasis by halting NF-κB signaling activation

We established an in situ HCC model by intrahepatic injection of Huh-7 cells and CAFs cells treated differently to investigate the impact of BMSCs-EVs-mediated regulation of B4GALT3/NF-κB pathway on CAFs activity in HCC tumor growth (Fig. 6A). Live imaging experiments illustrated that contrasted with the HCC + PBS group, tumor growth was noticeably inhibited in the HCC + EVs^{lv-NC} group, with a further enhancement of tumor suppression in the HCC + $EVs^{lv-B4GALT3}$ group. Conversely, the HCC + $EVs^{lv-B4GALT3}$ + TNFα group notably promoted tumor growth compared to the HCC + $EVs^{lv-B4GALT3}$ group (Fig. 6B-C). Additionally, H&E staining of tissue sections demonstrated that tumor infiltration and nuclear characteristics of tumor cells were prominently reduced in the HCC + EVs^{lv-NC} and HCC + $EVs^{lv-B4GALT3}$ groups, showing some restoration and improvement of cell morphology and structure compared to the HCC + PBS and HCC + $EVs^{lv-B4GALT3}$ + TNFα groups (Fig. 6D). These results indicate that BMSCs-EVs-mediated inhibition of CAFs activity through the B4GALT3/NF-κB pathway can effectively suppress HCC tumor growth.

Furthermore, Tunel staining unveiled an augmented count of TUNEL-positive cells in the HCC + EVs^{lv-NC} group in contrast with the HCC + PBS group, accompanied by a heightened presence of TUNEL-positive cells in the HCC + $EVs^{lv-B4GALT3}$ group. In contrast, the quantity of TUNEL-positive cells oticeably lessened in the HCC + $EVs^{lv-B4GALT3}$ + TNFα group in contrast with the HCC + $EVs^{lv-B4GALT3}$ group (Fig. 6E). IHC staining for Ki-67 showed a decreased area of Ki-67-positive regions in the HCC + EVs^{lv-NC} group in relation to the HCC + PBS group, with a further decrease in Ki-67-positive areas in the HCC + $EVs^{lv-B4GALT3}$ group. Conversely, the HCC + $EVs^{lv-B4GALT3}$ + TNFα group indicated a substantial escalation in the area of Ki-67-positive regions compared to the HCC + $EVs^{lv-B4GALT3}$ group (Fig. 6F). These findings suggest that BMSCs-EVs-mediated inhibition of CAFs activity through the B4GALT3/NF-κB pathway can suppress tumor cell apoptosis and promote proliferation.

Subsequently, we further validated the regulatory role of the B4GALT3/NF-κB pathway in HCC mice in vivo. Initially, WB results revealed that contrasted against the HCC + PBS group, the HCC + EvsIv-NC group upregulated the expression of B4GALT3 in tumor tissue while downregulating the expression of p-IκBα/IκBα and p-p65/p65 in the NF-κB signaling pathway. In the HCC + EvsIv-B4GALT3 group, the expression of B4GALT3 in tumor tissue was further upregulated compared to the HCC + EvsIv-NC group, leading to a significant downregulation of p-IκBα/IκBα and p-p65/p65 expression. In comparison to the HCC + EvsIv-B4GALT3 group, the HCC + EvsIv-B4GALT3 + TNFα group showed no significant changes in B4GALT3 expression in tumor tissue but exhibited a significant upregulation of p-IκBα/IκBα and p-p65/p65 expression in the NF-κB signaling pathway (Fig. 7A). Furthermore, IHC and IF staining outcomes indicated that when juxtaposed with the HCC + PBS group, the HCC + EvsIv-NC and HCC + EvsIv-B4GALT3 groups illustrated a further drop in the expression of p-p65 and nuclear translocation of p65 in tumor tissue, along with an upregulation in B4GALT3 expression. In contrast, the HCC + EvsIv-B4GALT3 + TNFα group illustrated a noteworthy surge in p-p65 expression and p65 nuclear translocation in tumor tissue, with no significant difference in B4GALT3 expression (Fig. 7B-C). These

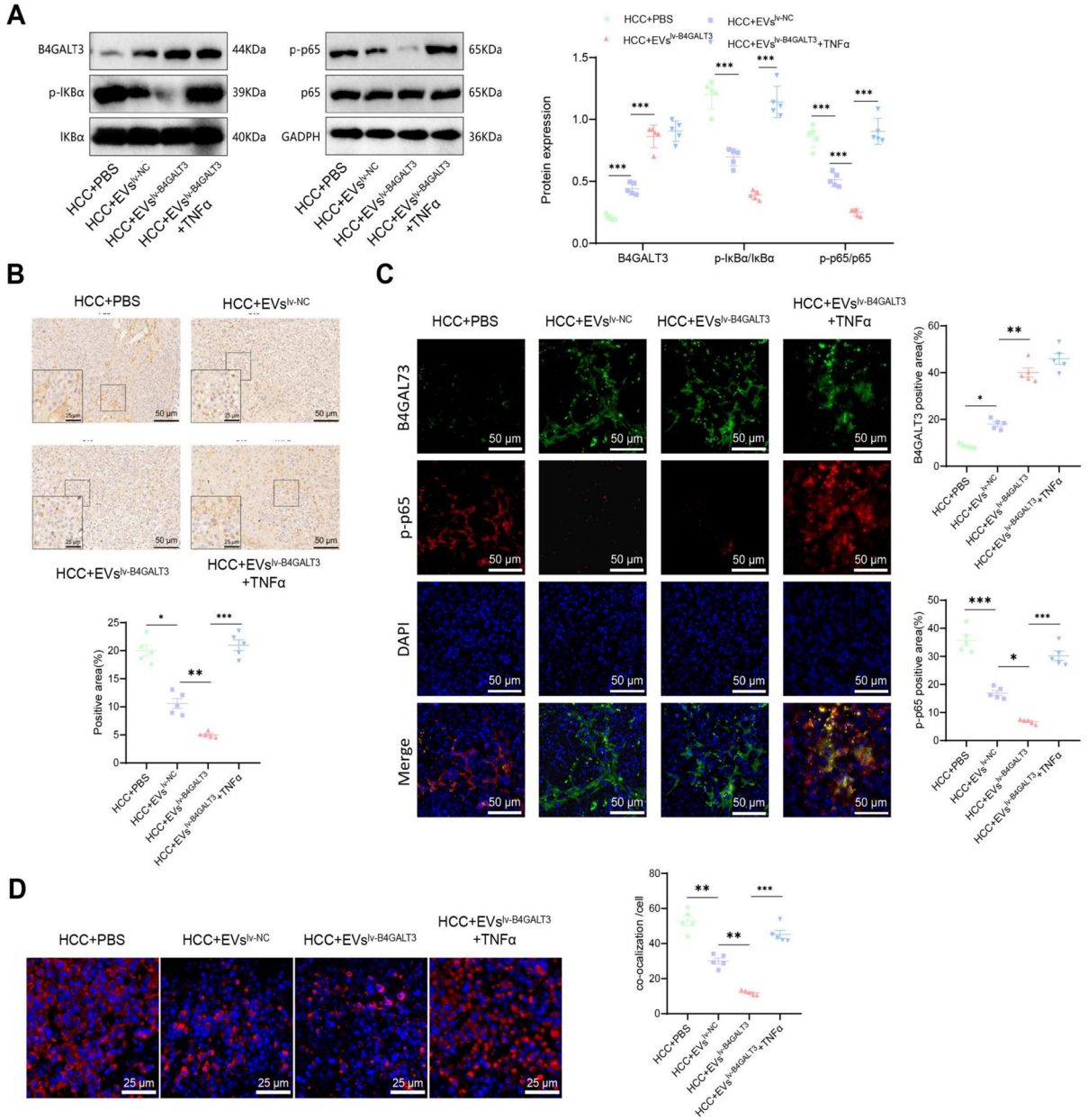

Fig. 7 Changes in the B4GALT3/NF-κB Signaling Pathway in HCC Mice. Note: (**A**) WB analysis of B4GALT3, p-IκBα, IκBα, p-p65, and p65 expression in tumors of each group of mice (n = 5). (**B**) IHC detection of p-p65 expression in tumor tissues of each group of mice (n = 5), with positive areas appearing light brown or dark brown, with a local enlargement in the lower left corner at a scale of 50 μm. (**C**) IF detection of B4GALT3 and p-p65 expression in tumor tissues of each group of mice (n = 5) at a scale of 50 μm. (**D**) IF staining of p65 in tumor tissues of each group of mice (n = 5) (scale = 25 μm), showing the fluorescence intensity of p65 co-localized with the cell nucleus in each cell, where p65 is shown in red and DAPI (cell nucleus) in blue. Numerical values are represented as mean ± standard deviation. * indicates $P < 0.05$, ** $P < 0.01$, *** $P < 0.001$

findings suggest that the inhibitory effect on HCC progression in HCC mice is related to the delivery of BAGALT3 into CAFs by BMSCs-EVs, inducing the obstruction of the NF-κB signaling pathway, consistent with the cellular observations (Fig. 7D).

Finally, we constructed a lung metastasis model of HCC by intravenously injecting Huh-7 cells and differently treated CAFs cells, to further evaluate the impact of MSCs-EVs-mediated B4GALT3/NF-κB pathway inhibition on CAFs activity in HCC mice (Fig. 8A). Contrasted with the HCC + PBS group, the quantity of lung metastatic nodules in mice was drastically minimized in the HCC + EvsIv-NC group, further lessened in the HCC + EvsIv-B4GALT3 group relative to the HCC + EvsIv-NC group. On the contrary, the HCC + EvsIv-B4GALT3 + TNFα group indicated a substantial escalation in the number of lung metastatic nodules in relation to the HCC + EvsIv-B4GALT3 group (Fig. 8B-C). Subsequently, IHC experiment outcomes illustrated that the HCC + EvsIv-NC group, contrasted against the HCC + PBS group, decreased the expression of N-cadherin and Vimentin in liver, while E-cadherin expression escalated. In the HCC + EvsIv-B4GALT3 group, the expression of N-cadherin and Vimentin in liver was further lessened contrasted with the HCC + EvsIv-NC group, with a noteworthy surge in E-cadherin expression. Lastly, when compared to the HCC + EvsIv-B4GALT3 group, the HCC + EvsIv-B4GALT3 + TNFα group exhibited a marked growth in the expression of N-cadherin and Vimentin in liver while showing a significant decrease in E-cadherin expression (Fig. 8D). Furthermore, IHC staining showed that, compared to the HCC + PBS group, the HCC + EVslv-NC group revealed reduced N-cadherin and Vimentin expression while increasing E-cadherin expression in lung tissue. In the HCC + EVslv-B4GALT3 group, N-cadherin and Vimentin expression was further reduced, while E-cadherin expression was substantially elevated relative to the HCC + EVslv-NC group. However, in the HCC + EVslv-B4GALT3 + TNFα group, N-cadherin and Vimentin expression significantly increased, whereas E-cadherin expression decreased (Fig. 8D-E). The data point towards BMSCs-EVs hindering the NF-κB signaling pathway activation through the transfer of B4GALT3, which effectively restrains CAFs activity, ultimately leading to the inhibition of lung metastasis in HCC mice.

Discussion

Recent studies have shown that BMSCs-EVs are crucial in promoting apoptosis and inhibiting tumor growth in HCC (Deng et al. 2021). The advancement and metastasis of HCC are propelled by the migration and invasion stimulation of HCC cells by CAFs through a variety of mechanisms (Xu et al. 2022; Liu et al. 2021; Zhu et al. 2023). Our groundbreaking research has revealed that BMSCs deliver B4GALT3 to the CAFs in the TME of HCC via EVs, thereby inhibiting their activation and impacting the development of HCC. This finding is innovative on multiple levels.

While previous studies have acknowledged the ability of BMSCs to regulate immune responses and secrete bioactive molecules, the specific mechanisms by which they alter the development of HCC by influencing CAFs in the TME remain limited (Zohora et al. 2023; Vaka et al. 2023). Focused on the delivery of B4GALT3, our study enhances the understanding of how BMSCs-EVs contribute to HCC development from a distinct standpoint.

Furthermore, our research delves into the critical role of B4GALT3 in regulating the activation of CAFs. Although B4GALT3 is implicated in the occurrence and progression of various cancers, its specific mechanism of action in HCC remains incompletely understood (Liu et al. 2018). We demonstrate that B4GALT3 hinders HCC progression by restraining the stimulation of CAFs within the TME, intricately linked to the blockage of the NF-κB signaling pathway. Previous research has revealed that miR-1247-3p targets B4GALT3 to activate the β1-integrin/NF-κB signaling pathway, leading to the activation of CAFs, promoting the progression and metastasis of HCC (Fang et al. 2018), consistent with our findings. Furthermore, B4GALT3-deficient fibroblasts secrete higher levels of IL-6 and IL-8, which are NF-κB pathway downstream targets. Increased secretion of these cytokines further activates the NF-κB pathway, forming a positive feedback loop that is pivotal in

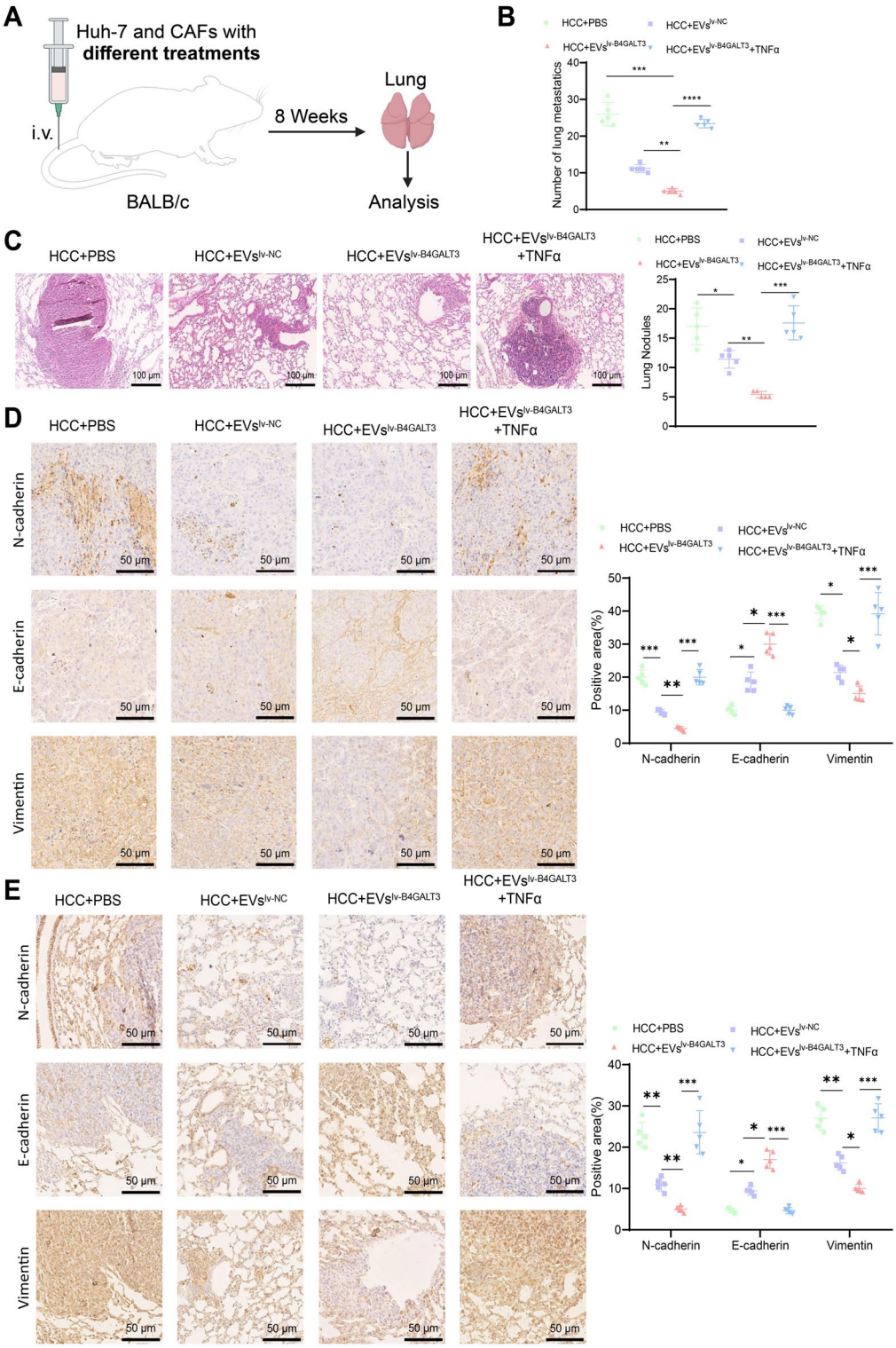
A
Huh-7 and CAFs with different treatments
i.v.
8 Weeks
Lung
BALB/c
Analysis
B
HCC+PBS
HCC+EVs lv-NC
HCC+EVs lv-B4GALT3
HCC+EVs lv-B4GALT3 +TNFα
Number of lung metastatics
C
HCC+PBS
HCC+EVs lv-NC
HCC+EVs lv-B4GALT3
HCC+EVs lv-B4GALT3 +TNFα
100 μm
Lung Nodules
D
N-cadherin
E-cadherin
Vimentin
50 μm
Positive area(%)
E
N-cadherin
E-cadherin
Vimentin
50 μm
Positive area(%)

◂**Fig. 8** Effects of CAFs with Different Treatments on the Lung Metastasis Model of HCC Mice. Note: (**A**) Schematic diagram illustrating the construction of the lung metastasis HCC model in mice where CAFs with different treatments were co-injected intravenously with Huh-7 cells; (**B**) Images of lungs from each group of mice (n = 5) with quantification of lung metastatic nodules; (**C**) H&E staining to evaluate the morphology and structure of lung tissues in each group of mice, scale bar = 100 μm; (**D**) IHC staining to assess the expression of E-cadherin, N-cadherin, and Vimentin in tumor cells in liver tissues of each group of mice, scale bar = 50 μm; (**E**) IHC staining to evaluate the expression of E-cadherin, N-cadherin, and Vimentin in lung tissues of each group of mice, scale bar = 50 μm; Values are presented as mean ± standard deviation, * indicates $P < 0.05$, ** indicates $P < 0.01$, *** indicates $P < 0.001$

inflammation and the TME (Liu et al. 2017). Additionally, studies have reported that in B4GALT3-deficient mice, CD8 + T cell infiltration and cytotoxic activity are enhanced, which may be associated with NF-κB pathway modulation. CD8 + T cells activate the NF-κB pathway by secreting cytokines such as IFN-γ and TNF-α. Therefore, B4GALT3 depletion may enhance CD8 + T cell activity, thereby affecting NF-κB downstream signaling (Wei et al. 2023). Our discovery emphasizes the role of BMSCs-EVs in modulating CAF behavior through the delivery of B4GALT3 to regulate the NF-κB signaling pathway, providing a new perspective on understanding its complex role in HCC.

In vitro experiments have demonstrated that the overexpression of B4GALT3 in BMSCs-EVs can further suppressed CAF viability,, thereby suppressing the migration and invasion of HCC cells. This finding is consistent with existing research, further confirming the significant role of B4GALT3 in tumor biology (Topno et al. 2021). In vivo animal experiments have shown that CAFs treated with BMSCs-EVs overexpressing B4GALT3 results in a remarkable suppression of HCC tumor growth and metastasis in mice. The authentication of this breakthrough corroborates the validity of the results attained through the in vitro studies.

Our research broadens the comprehension regarding the function of BMSCs-EVs in cancer therapy. Previous research has demonstrated that BMSCs can transfer various bioactive molecules via EVs, such as proteins, lipids, and RNA, altering the function of target cells (Chang et al. 2021; Yang et al. 2020; Orso et al. 2023). Our research reveals the significant impact of this transport mechanism on HCC development and highlights the potential therapeutic value of BMSCs-EVs as a treatment tool in HCC therapy. Our findings underscore the potential strategy of inhibiting HCC development by targeting CAF activation, providing a direction for developing novel treatment approaches.

Our study has shed new light on the role of BMSCs-EVs in HCC, but it is subject to certain limitations. Particularly, we have not directly demonstrated in vivo that BMSCs-EVs specifically act on CAFs within the TME or that the anti-tumor effects of BMSCs-EVs carrying B4GALT3 are solely dependent on CAF regulation. Moreover, while we have elucidated the potential mechanism by which BMSCs-EVs transport B4GALT3 to suppress CAF activation and consequently impact HCC development, these findings are predominantly based on in vitro and murine models and have yet to be validated in humans. Therefore, further research should investigate the in vivo mechanisms of BMSCs-EVs in the TME, and large-scale animal and clinical trials are necessary to validate these observations. Furthermore, our study did not clarify the mechanism by which BMSCs-EVs transport B4GALT3 to CAFs.

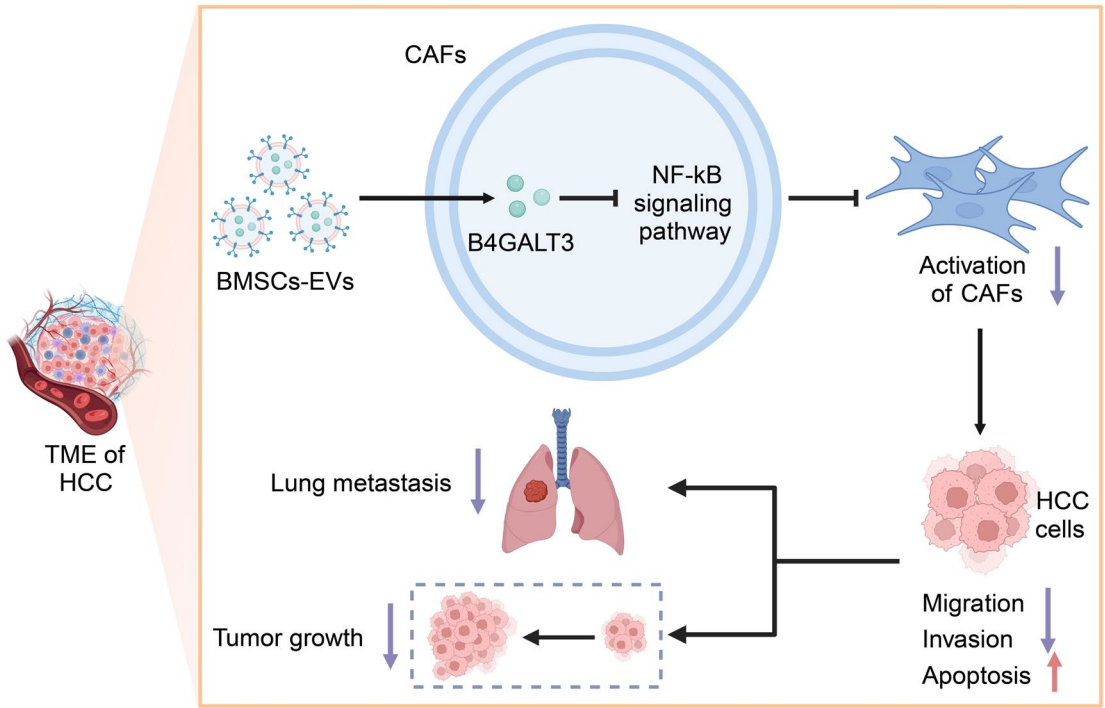

Fig. 9 Schematic Diagram of BMSCs-EVs Transporting B4GALT3 Mediating the Molecular Mechanism of NF-κB Signaling Pathway Involvement in HCC Growth and Metastasis

In summary, our investigation has revealed that BMSCs-EVs inhibit CAF activation by transporting B4GALT3 to suppress the NF-kB pathway, ultimately restraining HCC tumor growth and metastasis (Fig. 9). This discovery holds significant implications for understanding the mechanisms underlying HCC development and for identifying novel therapeutic approaches. Future research could delve deeper into the mechanisms through which BMSCs-EVs transport B4GALT3 to CAFs and further explore how B4GALT3 modulates CAF function by regulating the NF-κB pathway, thereby potentially uncovering new therapeutic targets for HCC treatment. Overall, examining the involvement of BMSCs-EVs in the progression of HCC, our research illuminates fresh insights and establishes a basis for the design of innovative treatment modalities informed by these findings.

Acknowledgements None.

Author contributions Juncheng Guo: Conceptualization, Methodology, Investigation, Data Curation, Writing—Original Draft. Kaiqiong Wang: Bioinformatic Analysis, Data Interpretation, Visualization, Writing—Review & Editing. Qigang Sun: Experimental Validation, Cell Culture, Western Blotting, Data Collection. Jun Liu: Transcriptome Sequencing, Statistical Analysis, Resources, Writing—Review & Editing. Jinfang Zheng: Supervision, Project Administration, Funding Acquisition, Writing—Review & Editing. All authors read and approved the final manuscript.

Funding This study was supported by 2023 Clinical Medical Research Center Project in Hainan Province (Project No. LCYX202302).

Data availability All data can be provided as needed.

Declarations

Ethical Statement All animal experiments were approved by the Animal Ethics Committee of Hainan General Hospital (No. [2022]298).

Conflict of Interest The authors declare no competing interests.

References

Abd-Allah SH, Shalaby SM, El-Shal AS, Elkader EA, Hussein S, Emam E, et al. Effect of bone marrow–derived mesenchymal stromal cells on hepatoma [Internet]. Cytotherapy. Elsevier BV; 2014 [cited 2025 Mar 5]. p. 1197–206. Available from: https://doi.org/10.1016/j.jcyt.2014.05.006

Affo S, Yu L-X, Schwabe RF. The Role of Cancer-Associated Fibroblasts and Fibrosis in Liver Cancer [Internet]. Annu. Rev. Pathol. Mech. Dis. Annual Reviews; 2017 [cited 2025 Mar 5]. p. 153–86. Available from: https://doi.org/10.1146/annurev-pathol-052016-100322

Andreeff M, Gaynor J, Chapman D, Little C, Gee T, Clarkson BD. Prognostic Factors in Acute Lymphoblastic Leukemia in Adults: The Memorial Hospital Experience [Internet]. Haematology and Blood Transfusion/Hämatologie und Bluttransfusion. Berlin, Heidelberg: Springer Berlin Heidelberg; 1987 [cited 2025 Mar 5]. p. 111–24. Available from: https://doi.org/10.1007/978-3-642-71213-5_18

Bai X, Zhou Y, Yokota Y, Matsumoto Y, Zhai B, Maarouf N, et al. Adaptive antitumor immune response stimulated by bio-nanoparticle based vaccine and checkpoint blockade [Internet]. J Exp Clin Cancer Res. Springer Science and Business Media LLC; 2022 [cited 2025 Mar 5]. Available from: https://doi.org/10.1186/s13046-022-02307-3

Biffi G, Tuveson DA. Diversity and Biology of Cancer-Associated Fibroblasts [Internet]. Physiological Reviews. American Physiological Society; 2021 [cited 2025 Mar 5]. p. 147–76. Available from: https://doi.org/10.1152/physrev.00048.2019

Bray F, Ferlay J, Soerjomataram I, Siegel RL, Torre LA, Jemal A. Global cancer statistics 2018: GLOBOCAN estimates of incidence and mortality worldwide for 36 cancers in 185 countries [Internet]. CA A Cancer J Clinicians. Wiley; 2018 [cited 2025 Mar 5]. p. 394–424. Available from: https://doi.org/10.3322/caac.21492

Cai Q, Shi P, Yuan Y, Peng J, Ou X, Zhou W, et al. Inflammation-Associated Senescence Promotes Helicobacter pylori–Induced Atrophic Gastritis [Internet]. Cellular and Molecular Gastroenterology and Hepatology. Elsevier BV; 2021 [cited 2025 Mar 5]. p. 857–80. Available from: https://doi.org/10.1016/j.jcmgh.2020.10.015

Chang X, Ma Z, Zhu G, Lu Y, Yang J. New perspective into mesenchymal stem cells: Molecular mechanisms regulating osteosarcoma [Internet]. Journal of Bone Oncology. Elsevier BV; 2021 [cited 2025 Mar 5]. p. 100372. Available from: https://doi.org/10.1016/j.jbo.2021.100372

Chen C-H, Wang S-H, Liu C-H, Wu Y-L, Wang W-J, Huang J, et al. β-1,4-Galactosyltransferase III suppresses β1 integrin-mediated invasive phenotypes and negatively correlates with metastasis in colorectal cancer [Internet]. Carcinogenesis. Oxford University Press (OUP); 2014 [cited 2025 Mar 5]. p. 1258–66. Available from: https://doi.org/10.1093/carcin/bgu007

Chen C, Cao M, Wu D, Li N, Peng J, Song L, et al. KH-type splicing regulatory protein mediate inflammatory response in gastric epithelial cells induced by lipopolysaccharide [Internet]. Cell Biology International. Wiley; 2017 [cited 2025 Mar 5]. p. 871–8. Available from: https://doi.org/10.1002/cbin.10804

Chen Z, Yang X, Bi G, Liang J, Hu Z, Zhao M, et al. Ligand-receptor interaction atlas within and between tumor cells and T cells in lung adenocarcinoma [Internet]. Int. J. Biol. Sci. Ivyspring International Publisher; 2020 [cited 2025 Mar 5]. p. 2205–19. Available from: https://doi.org/10.7150/ijbs.42080

Chidambaranathan-Reghupaty S, Fisher PB, Sarkar D. Hepatocellular carcinoma (HCC): Epidemiology, etiology and molecular classification [Internet]. Advances in Cancer Research. Elsevier; 2021 [cited 2025 Mar 5]. p. 1–61. Available from: https://doi.org/10.1016/bs.acr.2020.10.001

Cui Y, Wang D, Xie M. RETRACTED: Tumor-Derived Extracellular Vesicles Promote Activation of Carcinoma-Associated Fibroblasts and Facilitate Invasion and Metastasis of Ovarian Cancer by Carrying miR-630 [Internet]. Front. Cell Dev. Biol. Frontiers Media SA; 2021 [cited 2025 Mar 5]. Available from: https://doi.org/10.3389/fcell.2021.652322

Deng L, Wang C, He C, Chen L. Bone mesenchymal stem cells derived extracellular vesicles promote TRAIL-related apoptosis of hepatocellular carcinoma cells via the delivery of microRNA-20a-3p [Internet]. CBM. SAGE Publications; 2021 [cited 2025 Mar 5]. p. 223–35. Available from: https://doi.org/10.3233/cbm-201633

Dorronsoro A, Santiago FE, Grassi D, Zhang T, Lai RC, McGowan SJ, et al. Mesenchymal stem cell-derived extracellular vesicles reduce senescence and extend health span in mouse models of aging [Internet]. Aging Cell. Wiley; 2021 [cited 2025 Mar 5]. Available from: https://doi.org/10.1111/acel.13337

Du X, Qi H, Ji W, Li P, Hua R, Hu W, et al. Construction of a Colorectal Cancer Prognostic Risk Model and Screening of Prognostic Risk Genes Using Machine-Learning Algorithms [Internet]. Computational and Mathematical Methods in Medicine. Wiley; 2022 [cited 2025 Mar 5]. p. 1–20. Available from: https://doi.org/10.1155/2022/9408839

Eiro N, Fraile M, Fernández-Francos S, Sánchez R, Costa LA, Vizoso FJ. Importance of the origin of mesenchymal (stem) stromal cells in cancer biology: "alliance" or "war" in intercellular signals [Internet]. Cell Biosci. Springer Science and Business Media LLC; 2021 [cited 2025 Mar 5]. Available from: https://doi.org/10.1186/s13578-021-00620-6

Fang T, Lv H, Lv G, Li T, Wang C, Han Q, et al. Tumor-derived exosomal miR-1247-3p induces cancer-associated fibroblast activation to foster lung metastasis of liver cancer [Internet]. Nat Commun. Springer Science and Business Media LLC; 2018 [cited 2025 Mar 5]. Available from: https://doi.org/10.1038/s41467-017-02583-0

Gangadaran P, Rajendran RL, Lee HW, Kalimuthu S, Hong CM, Jeong SY, et al. Extracellular vesicles from mesenchymal stem cells activates VEGF receptors and accelerates recovery of hindlimb ischemia [Internet]. Journal of Controlled Release. Elsevier BV; 2017 [cited 2025 Mar 5]. p. 112–26. Available from: https://doi.org/10.1016/j.jconrel.2017.08.022

Gu H, Yan C, Wan H, Wu L, Liu J, Zhu Z, et al. Mesenchymal stem cell-derived exosomes block malignant behaviors of hepatocellular carcinoma stem cells through a lncRNA C5orf66-AS1/microRNA-127–3p/DUSP1/ERK axis [Internet]. Human Cell. Springer Science and Business Media LLC; 2021 [cited 2025 Mar 5]. p. 1812–29. Available from: https://doi.org/10.1007/s13577-021-00599-9

Guo M, Yin Z, Chen F, Lei P. Mesenchymal stem cell-derived exosome: a promising alternative in the therapy of Alzheimer's disease [Internet]. Alz Res Therapy. Springer Science and Business Media LLC; 2020 [cited 2025 Mar 5]. Available from: https://doi.org/10.1186/s13195-020-00670-x

Hack SP, Spahn J, Chen M, Cheng A-L, Kaseb A, Kudo M, et al. IMbrave 050: A Phase III Trial of Atezolizumab Plus Bevacizumab in High-Risk Hepatocellular Carcinoma after Curative Resection or Ablation [Internet]. Future Oncol. Informa UK Limited; 2020 [cited 2025 Mar 5]. p. 975–89. Available from: https://doi.org/10.2217/fon-2020-0162

Hanson D, Hoffman LM, Nagabushan S, Goumnerova LC, Rathmann A, Vogel T, et al. A modified IRS-III chemotherapy regimen leads to prolonged survival in children with embryonal tumor with multilayer rosettes [Internet]. Neuro-Oncology Advances. Oxford University Press (OUP); 2020 [cited 2025 Mar 5]. Available from: https://doi.org/10.1093/noajnl/vdaa120

Hayes JD, Dinkova-Kostova AT, Tew KD. Oxidative Stress in Cancer [Internet]. Cancer Cell. Elsevier BV; 2020 [cited 2025 Mar 5]. p. 167–97. Available from: https://doi.org/10.1016/j.ccell.2020.06.001

He L, Zhu C, Jia J, Hao X-Y, Yu X-Y, Liu X-Y, et al. ADSC-Exos containing MALAT1 promotes wound healing by targeting miR-124 through activating Wnt/β-catenin pathway [Internet]. Bioscience Reports. Portland Press Ltd.; 2020 [cited 2025 Mar 5]. Available from: 10.1042/bsr20192549

Hou P, Luo L, Chen H, Chen Q, Bian X, Wu S, et al. Ectosomal PKM2 Promotes HCC by Inducing Macrophage Differentiation and Remodeling the Tumor Microenvironment [Internet]. Molecular Cell. Elsevier BV; 2020 [cited 2025 Mar 5]. p. 1192–1206.e10. Available from: https://doi.org/10.1016/j.molcel.2020.05.004

Huang H, Wang Z, Zhang Y, Pradhan RN, Ganguly D, Chandra R, et al. Mesothelial cell-derived antigen-presenting cancer-associated fibroblasts induce expansion of regulatory T cells in pancreatic cancer [Internet]. Cancer Cell. Elsevier BV; 2022a [cited 2025 Mar 5]. p. 656–673.e7. Available from: https://doi.org/10.1016/j.ccell.2022.04.011

Huang L, Rong Y, Tang X, Yi K, Qi P, Hou J, et al. Engineered exosomes as an in situ DC-primed vaccine to boost antitumor immunity in breast cancer [Internet]. Mol Cancer. Springer Science and Business Media LLC; 2022b [cited 2025 Mar 5]. Available from: https://doi.org/10.1186/s12943-022-01515-x

Huang L, Xiong J, Fu J, Zhou Z, Yu H, Xu J, et al. (2022c) Bone marrow mesenchymal stem cell-derived exosomal LINC00847 inhibits the proliferation, migration, and invasion of Ewing sarcoma. J Clin Transl Res. Singapore; 24;8(6):563–76.

Hwang B, Engel L, Goueli SA, Zegzouti H. A homogeneous bioluminescent immunoassay to probe cellular signaling pathway regulation [Internet]. Commun Biol. Springer Science and Business Media LLC; 2020 [cited 2025 Mar 5]. Available from: https://doi.org/10.1038/s42003-019-0723-9

Jiang K, Dong C, Yin Z, Li R, Mao J, Wang C, et al. Exosome-derived ENO1 regulates integrin α6β4 expression and promotes hepatocellular carcinoma growth and metastasis [Internet]. Cell Death Dis. Springer Science and Business Media LLC; 2020 [cited 2025 Mar 5]. Available from: https://doi.org/10.1038/s41419-020-03179-1

Jin Z, Ren J, Qi S. Exosomal miR-9–5p secreted by bone marrow–derived mesenchymal stem cells alleviates osteoarthritis by inhibiting syndecan-1 [Internet]. Cell Tissue Res. Springer Science and Business Media LLC; 2020 [cited 2025 Mar 5]. p. 99–114. Available from: https://doi.org/10.1007/s00441-020-03193-x

Khan F, Pang L, Dunterman M, Lesniak MS, Heimberger AB, Chen P. Macrophages and microglia in glioblastoma: heterogeneity, plasticity, and therapy [Internet]. Journal of Clinical Investigation. American Society for Clinical Investigation; 2023 [cited 2025 Mar 5]. Available from: https://doi.org/10.1172/jci163446

Kletukhina S, Mutallapova G, Titova A, Gomzikova M. Role of Mesenchymal Stem Cells and Extracellular Vesicles in Idiopathic Pulmonary Fibrosis [Internet]. IJMS. MDPI AG; 2022 [cited 2025 Mar 5]. p. 11212. Available from: https://doi.org/10.3390/ijms231911212

Konyn P, Ahmed A, Kim D. Current epidemiology in hepatocellular carcinoma [Internet]. Expert Review of Gastroenterology & Hepatology. Informa UK Limited; 2021 [cited 2025 Mar 5]. p. 1295–307. Available from: https://doi.org/10.1080/17474124.2021.1991792

Langfelder P, Horvath S. WGCNA: an R package for weighted correlation network analysis [Internet]. BMC Bioinformatics. Springer Science and Business Media LLC; 2008 [cited 2025 Mar 5]. Available from: https://doi.org/10.1186/1471-2105-9-559

Lazarian G, Friedrich C, Quinquenel A, Tran J, Ouriemmi S, Dondi E, et al. Stabilization of β-catenin upon B-cell receptor signaling promotes NF-kB target genes transcription in mantle cell lymphoma [Internet]. Oncogene. Springer Science and Business Media LLC; 2020 [cited 2025 Mar 5]. p. 2934–47. Available from: https://doi.org/10.1038/s41388-020-1183-x

Li Y, Zhang J, Shi J, Liu K, Wang X, Jia Y, et al. Exosomes derived from human adipose mesenchymal stem cells attenuate hypertrophic scar fibrosis by miR-192-5p/IL-17RA/Smad axis [Internet]. Stem Cell Res Ther. Springer Science and Business Media LLC; 2021 [cited 2025 Mar 5]. Available from: https://doi.org/10.1186/s13287-021-02290-0

Li W, Liu D, Xu J, Zha J, Wang C, An J, et al. Astrocyte-Derived TNF-α-Activated Platelets Promote Cerebral Ischemia/Reperfusion Injury by Regulating the RIP1/RIP3/AKT Signaling Pathway [Internet]. Mol Neurobiol. Springer Science and Business Media LLC; 2022a [cited 2025 Mar 5]. p. 5734–49. Available from: https://doi.org/10.1007/s12035-022-02942-z

Li X, Sun Z, Peng G, Xiao Y, Guo J, Wu B, et al. Single-cell RNA sequencing reveals a pro-invasive cancer-associated fibroblast subgroup associated with poor clinical outcomes in patients with gastric cancer [Internet]. Theranostics. Ivyspring International Publisher; 2022b [cited 2025 Mar 5]. p. 620–38. Available from: https://doi.org/10.7150/thno.60540

Liang N, Li Y, Chung HY. Two natural eudesmane-type sesquiterpenes from Laggera alata inhibit angiogenesis and suppress breast cancer cell migration through VEGF- and Angiopoietin 2-mediated signaling pathways [Internet]. International Journal of Oncology. Spandidos Publications; 2017 [cited 2025 Mar 5]. p. 213–22. Available from: https://doi.org/10.3892/ijo.2017.4004

Liang X, Cheng Z, Chen X, Li J. Prognosis analysis of necroptosis-related genes in colorectal cancer based on bioinformatic analysis [Internet]. Front. Genet. Frontiers Media SA; 2022 [cited 2025 Mar 5]. Available from: https://doi.org/10.3389/fgene.2022.955424

Lin L, Chen S, Wang H, Gao B, Kallakury B, Bhuvaneshwar K, et al. SPTBN1 inhibits inflammatory responses and hepatocarcinogenesis via the stabilization of SOCS1 and downregulation of p65 in hepatocellular carcinoma [Internet]. Theranostics. Ivyspring International Publisher; 2021 [cited 2025 Mar 5]. p. 4232–50. Available from: https://doi.org/10.7150/thno.49819

Liu T, Zhang L, Joo D, Sun S-C. NF-κB signaling in inflammation [Internet]. Sig Transduct Target Ther. Springer Science and Business Media LLC; 2017 [cited 2025 Mar 5]. Available from: https://doi.org/10.1038/sigtrans.2017.23

Liu H, Chen D, Bi J, Han J, Yang M, Dong W, et al. Circular RNA circUBXN7 represses cell growth and invasion by sponging miR-1247–3p to enhance B4GALT3 expression in bladder cancer [Internet]. Aging. Impact Journals, LLC; 2018 [cited 2025 Mar 5]. p. 2606–23. Available from: https://doi.org/10.18632/aging.101573

Liu G, Sun J, Yang Z-F, Zhou C, Zhou P-Y, Guan R-Y, et al. Cancer-associated fibroblast-derived CXCL11 modulates hepatocellular carcinoma cell migration and tumor metastasis through the circUBAP2/miR-4756/IFIT1/3 axis [Internet]. Cell Death Dis. Springer Science and Business Media LLC; 2021 [cited 2025 Mar 5]. Available from: https://doi.org/10.1038/s41419-021-03545-7

Liu Y, Zhang L, Ju X, Wang S, Qie J. Single-Cell Transcriptomic Analysis Reveals Macrophage–Tumor Crosstalk in Hepatocellular Carcinoma [Internet]. Front. Immunol. Frontiers Media SA; 2022 [cited 2025 Mar 5]. Available from: https://doi.org/10.3389/fimmu.2022.955390

Llovet JM, Kelley RK, Villanueva A, Singal AG, Pikarsky E, Roayaie S, et al. Hepatocellular carcinoma [Internet]. Nat Rev Dis Primers. Springer Science and Business Media LLC; 2021 [cited 2025 Mar 5]. Available from: https://doi.org/10.1038/s41572-020-00240-3

Luo H, Xia X, Huang L-B, An H, Cao M, Kim GD, et al. Pan-cancer single-cell analysis reveals the heterogeneity and plasticity of cancer-associated fibroblasts in the tumor microenvironment [Internet]. Nat Commun. Springer Science and Business Media LLC; 2022 [cited 2025 Mar 5]. Available from: https://doi.org/10.1038/s41467-022-34395-2

Mao C, Li D, Zhou E, Zhang J, Wang C, Xue C. Nicotine exacerbates atherosclerosis through a macrophage-mediated endothelial injury pathway [Internet]. Aging. Impact Journals, LLC; 2021a [cited 2025 Mar 5]. p. 7627–43. Available from: https://doi.org/10.18632/aging.202660

Mao X, Xu J, Wang W, Liang C, Hua J, Liu J, et al. Crosstalk between cancer-associated fibroblasts and immune cells in the tumor microenvironment: new findings and future perspectives [Internet]. Mol Cancer. Springer Science and Business Media LLC; 2021b [cited 2025 Mar 5]. Available from: https://doi.org/10.1186/s12943-021-01428-1

Nevola R, Ruocco R, Criscuolo L, Villani A, Alfano M, Beccia D, et al. Predictors of early and late hepatocellular carcinoma recurrence [Internet]. World J Gastroenterol. Baishideng Publishing Group Inc.; 2023 [cited 2025 Mar 5]. p. 1243–60. Available from: https://doi.org/10.3748/wjg.v29.i8.1243

Ni H, Qin H, Sun C, Liu Y, Ruan G, Guo Q, et al. MiR-375 reduces the stemness of gastric cancer cells through triggering ferroptosis [Internet]. Stem Cell Res Ther. Springer Science and Business Media LLC; 2021 [cited 2025 Mar 5]. Available from: https://doi.org/10.1186/s13287-021-02394-7

Orso F, Virga F, Dettori D, Dalmasso A, Paradzik M, Savino A, et al. Stroma-derived miR-214 coordinates tumor dissemination [Internet]. J Exp Clin Cancer Res. Springer Science and Business Media LLC; 2023 [cited 2025 Mar 5]. Available from: https://doi.org/10.1186/s13046-022-02553-5

Peng C, Ouyang Y, Lu N, Li N. The NF-κB Signaling Pathway, the Microbiota, and Gastrointestinal Tumorigenesis: Recent Advances [Internet]. Front. Immunol. Frontiers Media SA; 2020 [cited 2025 Mar 5]. Available from: https://doi.org/10.3389/fimmu.2020.01387

Peng R, Lin H, Zhu H, Zhang Y, Bao T, Li W, et al. Involvement of IGF1 in endoplasmic reticulum stress contributes to cataract formation through regulating Nrf2/NF-κB signaling [Internet]. Funct Integr Genomics. Springer Science and Business Media LLC; 2023 [cited 2025 Mar 5]. Available from: https://doi.org/10.1007/s10142-023-01152-7

Salah RA, Nasr MA, El-Derby AM, Abd Elkodous M, Mohamed RH, El-Ekiaby N, et al. Hepatocellular carcinoma cell line-microenvironment induced cancer-associated phenotype, genotype and functionality in mesenchymal stem cells [Internet]. Life Sciences. Elsevier BV; 2022 [cited 2025 Mar 5]. p. 120168. Available from: https://doi.org/10.1016/j.lfs.2021.120168

Shi L, Chen H, Qin Y-Y, Gan T-Q, Wei K-L. Clinical and biologic roles of PDGFRA in papillary thyroid cancer: a study based on immunohistochemical and in vitro analyses. Int J Clin Exp Pathol. United States; 2020 May 1;13(5):1094–107.

Song J, Shawky JH, Kim Y, Hazar M, LeDuc PR, Sitti M, et al. Controlled surface topography regulates collective 3D migration by epithelial–mesenchymal composite embryonic tissues [Internet]. Biomaterials. Elsevier BV; 2015 [cited 2025 Mar 5]. p. 1–9. Available from: https://doi.org/10.1016/j.biomaterials.2015.04.021

Sun B, Lei X, Cao M, Li Y, Yang L-Y. Hepatocellular carcinoma cells remodel the pro-metastatic tumour microenvironment through recruitment and activation of fibroblasts via paracrine Egfl7 signaling [Internet]. Cell Commun Signal. Springer Science and Business Media LLC; 2023 [cited 2025 Mar 5]. Available from: https://doi.org/10.1186/s12964-023-01200-6

Tang Q, Ma Z, Tang X, Liu Y, Wu H, Peng Y, et al. Coptisine inhibits Helicobacter pylori and reduces the expression of CagA to alleviate host inflammation in vitro and in vivo [Internet]. Journal of Ethnopharmacology. Elsevier BV; 2023 [cited 2025 Mar 5]. p. 116618. Available from: https://doi.org/10.1016/j.jep.2023.116618

Taniue K, Kurimoto A, Takeda Y, Nagashima T, Okada-Hatakeyama M, Katou Y, et al. ASBEL –TCF3 complex is required for the tumorigenicity of colorectal cancer cells [Internet]. Proc. Natl. Acad. Sci. U.S.A. Proceedings of the National Academy of Sciences; 2016 [cited 2025 Mar 5]. p. 12739–44. Available from: https://doi.org/10.1073/pnas.1605938113

Topno R, Singh I, Kumar M, Agarwal P. Integrated bioinformatic analysis identifies UBE2Q1 as a potential prognostic marker for high grade serous ovarian cancer [Internet]. BMC Cancer. Springer Science and Business Media LLC; 2021 [cited 2025 Mar 5]. Available from: https://doi.org/10.1186/s12885-021-07928-z

Vaka R, Parent S, Risha Y, Khan S, Courtman D, Stewart DJ, et al. Extracellular vesicle microRNA and protein cargo profiling in three clinical-grade stem cell products reveals key functional pathways [Internet]. Molecular Therapy - Nucleic Acids. Elsevier BV; 2023 [cited 2025 Mar 5]. p. 80–93. Available from: https://doi.org/10.1016/j.omtn.2023.03.001

de Visser KE, Joyce JA. The evolving tumor microenvironment: From cancer initiation to metastatic outgrowth [Internet]. Cancer Cell. Elsevier BV; 2023 [cited 2025 Mar 5]. p. 374–403. Available from: https://doi.org/10.1016/j.ccell.2023.02.016

Vogel A, Meyer T, Sapisochin G, Salem R, Saborowski A. Hepatocellular carcinoma [Internet]. The Lancet. Elsevier BV; 2022 [cited 2025 Mar 5]. p. 1345–62. Available from: https://doi.org/10.1016/s0140-6736(22)01200-4

Vucur M, Ghallab A, Schneider AT, Adili A, Cheng M, Castoldi M, et al. Sublethal necroptosis signaling promotes inflammation and liver cancer [Internet]. Immunity. Elsevier BV; 2023 [cited 2025 Mar 5]. p. 1578–1595.e8. Available from: https://doi.org/10.1016/j.immuni.2023.05.017

Wan W, Wang L, Liu Y, Hu Y. Improving the detection of Helicobacter pylori in biopsies of chronic gastritis: a comparative analysis of H&E, methylene blue, Warthin-Starry, immunohistochemistry, and quantum dots immunohistochemistry [Internet]. Front. Oncol. Frontiers Media SA; 2023 [cited 2025 Mar 5]. Available from: https://doi.org/10.3389/fonc.2023.1229871

Wang Y, Zhou Z, Liu Y, Wang Z, Kang Y. Inhibition of Smad3 promotes the healing of rotator cuff injury in a rat model [Internet]. Journal Orthopaedic Research. Wiley; 2020 [cited 2025 Mar 5]. p. 204–18. Available from: https://doi.org/10.1002/jor.24768

Wang W, Peng X, Zhao L, Zhao H, Gu Q. Extracellular Vesicles From Bone Marrow Mesenchymal Stem Cells InhibitApoptosis and Autophagy of Ischemia-hypoxia Cardiomyocyte Line invitro by Carrying miR-144–3p to Inhibit ROCK1 [Internet]. CSCR. Bentham Science Publishers Ltd.; 2023 [cited 2025 Mar 5]. p. 247–59. Available from: https://doi.org/10.2174/1574888x17666220503192941

Wei H, Naruse C, Takakura D, Sugihara K, Pan X, Ikeda A, et al. Beta-1,4-galactosyltransferase-3 deficiency suppresses the growth of immunogenic tumors in mice [Internet]. Front. Immunol. Frontiers Media SA; 2023 [cited 2025 Mar 5]. Available from: https://doi.org/10.3389/fimmu.2023.1272537

Xiong W-P, Yao W-Q, Wang B, Liu K. BMSCs-exosomes containing GDF-15 alleviated SH-SY5Y cell injury model of Alzheimer's disease via AKT/GSK-3β/β-catenin [Internet]. Brain Research Bulletin. Elsevier BV; 2021 [cited 2025 Mar 5]. p. 92–102. Available from: https://doi.org/10.1016/j.brainresbull.2021.09.008

Xiong H, Ye J, Xie K, Hu W, Xu N, Yang H. Exosomal IL-8 derived from Lung Cancer and Colon Cancer cells induced adipocyte atrophy via NF-κB signaling pathway [Internet]. Lipids Health Dis. Springer Science and Business Media LLC; 2022 [cited 2025 Mar 5]. Available from: https://doi.org/10.1186/s12944-022-01755-2

Xu X, Lei Y, Chen L, Zhou H, Liu H, Jiang J, et al. Phosphorylation of NF-κBp65 drives inflammation-mediated hepatocellular carcinogenesis and is a novel therapeutic target [Internet]. J Exp Clin Cancer Res. Springer Science and Business Media LLC; 2021 [cited 2025 Mar 5]. Available from: https://doi.org/10.1186/s13046-021-02062-x

Xu H, Zhao J, Li J, Zhu Z, Cui Z, Liu R, et al. Cancer associated fibroblast–derived CCL5 promotes hepatocellular carcinoma metastasis through activating HIF1α/ZEB1 axis [Internet]. Cell Death Dis. Springer Science and Business Media LLC; 2022 [cited 2025 Mar 5]. Available from: https://doi.org/10.1038/s41419-022-04935-1

Yang E, Wang X, Gong Z, Yu M, Wu H, Zhang D. Exosome-mediated metabolic reprogramming: the emerging role in tumor microenvironment remodeling and its influence on cancer progression [Internet]. Sig Transduct Target Ther. Springer Science and Business Media LLC; 2020 [cited 2025 Mar 5]. Available from: https://doi.org/10.1038/s41392-020-00359-5

Yang M, Li J, Gu P, Fan X. The application of nanoparticles in cancer immunotherapy: Targeting tumor microenvironment [Internet]. Bioactive Materials. Elsevier BV; 2021 [cited 2025 Mar 5]. p. 1973–87. Available from: https://doi.org/10.1016/j.bioactmat.2020.12.010

Yang C, Guan Z, Pang X, Tan Z, Yang X, Li X, et al. Desialylated Mesenchymal Stem Cells-Derived Extracellular Vesicles Loaded with Doxorubicin for Targeted Inhibition of Hepatocellular Carcinoma [Internet]. Cells. MDPI AG; 2022 [cited 2025 Mar 5]. p. 2642. Available from: https://doi.org/10.3390/cells11172642

Yin Z, Dong C, Jiang K, Xu Z, Li R, Guo K, et al. Heterogeneity of cancer-associated fibroblasts and roles in the progression, prognosis, and therapy of hepatocellular carcinoma [Internet]. J Hematol Oncol. Springer Science and Business Media LLC; 2019 [cited 2025 Mar 5]. Available from: https://doi.org/10.1186/s13045-019-0782-x

Yu H, Lin L, Zhang Z, Zhang H, Hu H. Targeting NF-κB pathway for the therapy of diseases: mechanism and clinical study [Internet]. Sig Transduct Target Ther. Springer Science and Business Media LLC; 2020 [cited 2025 Mar 5]. Available from: https://doi.org/10.1038/s41392-020-00312-6

Yue B, Song C, Yang L, Cui R, Cheng X, Zhang Z, et al. METTL3-mediated N6-methyladenosine modification is critical for epithelial-mesenchymal transition and metastasis of gastric cancer [Internet]. Mol Cancer. Springer Science and Business Media LLC; 2019 [cited 2025 Mar 5]. Available from: https://doi.org/10.1186/s12943-019-1065-4

Zhang Z, Wang J, Chen Y, Suo L, Chen H, Zhu L, et al. Activin a promotes myofibroblast differentiation of endometrial mesenchymal stem cells via STAT3-dependent Smad/CTGF pathway [Internet]. Cell Commun Signal. Springer Science and Business Media LLC; 2019 [cited 2025 Mar 5]. Available from: https://doi.org/10.1186/s12964-019-0361-3

Zhang W, Zhang B, Chen X. Adjuvant treatment strategy after curative resection for hepatocellular carcinoma [Internet]. Front. Med. Springer Science and Business Media LLC; 2021a [cited 2025 Mar 5]. p. 155–69. Available from: https://doi.org/10.1007/s11684-021-0848-3

Zhang W, Zhangyuan G, Wang F, Jin K, Shen H, Zhang L, et al. The zinc finger protein Miz1 suppresses liver tumorigenesis by restricting hepatocyte-driven macrophage activation and inflammation [Internet]. Immunity. Elsevier BV; 2021b [cited 2025 Mar 5]. p. 1168–1185.e8. Available from: https://doi.org/10.1016/j.immuni.2021.04.027

Zhang X, Li N, Zhu Y, Wen W. The role of mesenchymal stem cells in the occurrence, development, and therapy of hepatocellular carcinoma [Internet]. Cancer Medicine. Wiley; 2022 [cited 2025 Mar 5]. p. 931–43. Available from: https://doi.org/10.1002/cam4.4521

Zhang L. The Role of Mesenchymal Stem Cells in Modulating the Breast Cancer Microenvironment [Internet]. Cell Transplant. SAGE Publications; 2023 [cited 2025 Mar 5]. Available from: https://doi.org/10.1177/09636897231220073

Zhao H, Wu L, Yan G, Chen Y, Zhou M, Wu Y, et al. Inflammation and tumor progression: signaling pathways and targeted intervention [Internet]. Sig Transduct Target Ther. Springer Science and Business Media LLC; 2021 [cited 2025 Mar 5]. Available from: https://doi.org/10.1038/s41392-021-00658-5

Zhao J, Li R, Li J, Chen Z, Lin Z, Zhang B, et al. CAFs-derived SCUBE1 promotes malignancy and stemness through the Shh/Gli1 pathway in hepatocellular carcinoma [Internet]. J Transl Med. Springer Science and Business Media LLC; 2022 [cited 2025 Mar 5]. Available from: https://doi.org/10.1186/s12967-022-03689-w

Zheng W, Yang Y, Sequeira RC, Bishop CE, Atala A, Gu Z, et al. Effects of Extracellular Vesicles Derived from Mesenchymal Stem/Stromal Cells on Liver Diseases [Internet]. CSCR. Bentham Science Publishers Ltd.; 2019 [cited 2025 Mar 5]. p. 442–52. Available from: https://doi.org/10.2174/1574888x14666190308123714

Zhou X, Chu X, Yuan H, Qiu J, Zhao C, Xin D, et al. Mesenchymal stem cell derived EVs mediate neuroprotection after spinal cord injury in rats via the microRNA-21–5p/FasL gene axis [Internet]. Biomedicine & Pharmacotherapy. Elsevier BV; 2019 [cited 2025 Mar 5]. p. 108818. Available from: https://doi.org/10.1016/j.biopha.2019.108818

Zhou C, Zhang B, Yang Y, Jiang Q, Li T, Gong J, et al. Stem cell-derived exosomes: emerging therapeutic opportunities for wound healing [Internet]. Stem Cell Res Ther. Springer Science and Business Media LLC; 2023 [cited 2025 Mar 5]. Available from: https://doi.org/10.1186/s13287-023-03345-0

Zhu L, Yang X, Feng J, Mao J, Zhang Q, He M, et al. CYP2E1 plays a suppressive role in hepatocellular carcinoma by regulating Wnt/Dvl2/β-catenin signaling [Internet]. J Transl Med. Springer Science and Business Media LLC; 2022 [cited 2025 Mar 5]. Available from: https://doi.org/10.1186/s12967-022-03396-6

Zhu G-Q, Tang Z, Huang R, Qu W-F, Fang Y, Yang R, et al. CD36+ cancer-associated fibroblasts provide immunosuppressive microenvironment for hepatocellular carcinoma via secretion of macrophage migration inhibitory factor [Internet]. Cell Discov. Springer Science and Business Media LLC; 2023 [cited 2025 Mar 5]. Available from: https://doi.org/10.1038/s41421-023-00529-z

Zohora FT, Aliyu M, Saboor-Yaraghi AA. Secretome-based acellular therapy of bone marrow-derived mesenchymal stem cells in degenerative and immunological disorders: A narrative review [Internet]. Heliyon. Elsevier BV; 2023 [cited 2025 Mar 5]. p. e18120. Available from: https://doi.org/10.1016/j.heliyon.2023.e18120

Zou S, Wang C, Cui Z, Guo P, Meng Q, Shi X, et al. β-Elemene induces apoptosis of human rheumatoid arthritis fibroblast-like synoviocytes via reactive oxygen species-dependent

activation of p38 mitogen-activated protein kinase [Internet]. Pharmacological Reports. Springer Science and Business Media LLC; 2016 [cited 2025 Mar 5]. p. 7–11. Available from: https://doi.org/10.1016/j.pharep.2015.06.004

Zuo X, Chen Z, Gao W, Zhang Y, Wang J, Wang J, et al. M6A-mediated upregulation of LINC00958 increases lipogenesis and acts as a nanotherapeutic target in hepatocellular carcinoma [Internet]. J Hematol Oncol. Springer Science and Business Media LLC; 2020 [cited 2025 Mar 5]. Available from: https://doi.org/10.1186/s13045-019-0839-x

Zuo W, Yang H, Li N, Ouyang Y, Xu X, Hong J. Helicobacter pylori infection activates Wnt/β-catenin pathway to promote the occurrence of gastritis by upregulating ASCL1 and AQP5 [Internet]. Cell Death Discov. Springer Science and Business Media LLC; 2022 [cited 2025 Mar 5]. Available from: https://doi.org/10.1038/s41420-022-01026-0